Journal of Photochemistry and Photobiology C: Photochemistry Reviews 13 (2012) 28–54

Contents lists available at SciVerse ScienceDirect

Journal of Photochemistry and Photobiology C: Photochemistry Reviews

journal homepage: www.elsevier.com/locate/jphotochemrev

Invited review

Studies on the interaction of pulsed lasers with plasmonic gold nanoparticles toward light manipulation, heat management, and nanofabrication

Shuichi Hashimoto[a,*], Daniel Werner[a], Takayuki Uwada[b]

[a] Department of Ecosystem Engineering, The University of Tokushima, Tokushima 770-8506, Japan
[b] Department of Applied Chemistry and Institute of Molecular Science, National Chiao Tung University, Hsinchu 30010, Taiwan

ARTICLE INFO

Article history:
Received 5 December 2011
Received in revised form 18 January 2012
Accepted 23 January 2012
Available online 2 February 2012

Keywords:
Gold nanoparticles
Laser-induced size reduction
Surface plasmon resonance
Photothermal response
Plasmonic nanobubble

ABSTRACT

This review describes the fundamental aspects of laser–gold nanoparticle (Au NP) interaction that leads to nanoscale energy deposition to the surroundings through light amplification and heat generation. Besides the importance of the primary process in physics and chemistry, application of the light–NP interaction has attracted significant interest from various areas ranging from analytical chemistry to material chemistry and biomedicine. Here we consider both mechanistic and application aspects. Our attention is focused on pulsed-laser-induced fast processes that revealed the heating–cooling dynamics of electrons, lattice (particle), and particle's environment. On the application side, we focus on material fabrication and processing that beat diffraction-limited resolution. Together, we will shed a light on the essence of research activities carried out in the past 10 years. In addition to an abundance of latest information obtained from currently available literature, this review includes figures obtained by our own calculations to provide readers with a better understanding of the basics of the optical properties and energy and heat-transfer processes of Au NPs, which are not familiar to photochemists.

Contents

* Corresponding author. Tel.: +81 88 656 7389; fax: +81 88 656 7598.
E-mail address: hashi@eco.tokushima-u.ac.jp (S. Hashimoto).

1389-5567/$20.00 © 2012 Elsevier B.V. All rights reserved.
doi:10.1016/j.jphotochemrev.2012.01.001

Shuichi Hashimoto has been a Professor of Ecosystem Engineering, at the Graduate School of Technology and Science, The University of Tokushima, Japan since 2005. He received a PhD in Physical Chemistry from Tokyo Metropolitan University in 1982 and carried out postdoctoral research at the University of Notre Dame under J.K. Thomas from 1982 to 1985. He worked with H. Masuhara as a visiting scholar at Osaka University, investigating the transient-absorption spectroscopy of zeolites in 1993. His current research interests are laser-induced size and shape transformations of plasmonic nanoparticles, microscopy–spectroscopy study of nanoparticles and nanostructures, femtosecond-laser processing of transparent solids, and optical microscopy study of zeolite photochemistry.

Daniel Werner, native of Dresden, Germany, is currently a JSPS postdoctoral fellow at The University of Tokushima. He received PhD in Physical Engineering from The University of Tokushima working with Prof. S. Hashimoto. His current research interest focuses on the nonlinear optical properties of multilayered core–shell nanoparticles, electron dynamics and thermodynamics of laser-heated nanoparticles in liquids, fragmentation mechanisms of noble metal nanoparticles and nanoparticle generation in liquids through a pulsed-laser-ablation technique.

Takayuki Uwada received a PhD in Applied Physics from Osaka University under the guidance of Prof. T. Asahi and Prof. H. Masuhara in 2007. After a year of postdoctoral research at the Hamano Life Science Research Foundation in Kobe, he has been appointed as an assistant research fellow in the Department of Applied Chemistry and Institute of Molecular Science, National Chiao Tung University, Taiwan under the guidance of Prof. Masuhara. His current research interests include static and dynamic light-scattering-microspectroscopy investigations of nanomaterials, laser-induced molecular/nanoparticle assembly and crystallization, and metallic nanoparticle plasmon application to biophysics.

1. Introduction

Past decades have witnessed an ever increasing interest in the optical properties of nanoparticles and nanostructures [1–7], which has had a tremendous impact on broad areas of research such as optics, electronics, biomedicine, analytical chemistry, and photochemistry. Scheme 1 gives an overview of the areas of current promising applications of plasmonic nanoparticles (NPs).

In nano-optics and nanoelectronics, miniaturization with high throughput is highly desirable; consequently, an interest in surface plasmons in optical circuits below the diffraction limit has grown rapidly [8,9]. In biomedical applications, because of their strongly resonant light-absorbing and light-scattering properties, plasmonic NPs can be useful contrast agents in the diagnostic imaging of tumors [10,11]. In addition, when illuminated, plasmonic NPs can serve as nanoscale heat sources, photothermally inducing cell death and tumor remission [12,13]. In chemistry, in particular for analytical applications, surface-enhanced Raman scattering spectroscopy (SERS) utilizing enhanced local electromagnetic fields near the plasmonic NPs and nanostructures is a promising tool for ultratrace analysis, ultimately enabling detection at the single-molecule level [14,15]. Biosensing that exploits the detection of a refractive-index change around the plasmonic NPs is another area of development [16–18]. Recent developments have greatly improved the sensitivity of plasmon sensors based on the single NPs and NP arrays. In the plasmonic NP field, photochemistry is currently prominent among the areas receiving increasing attention.

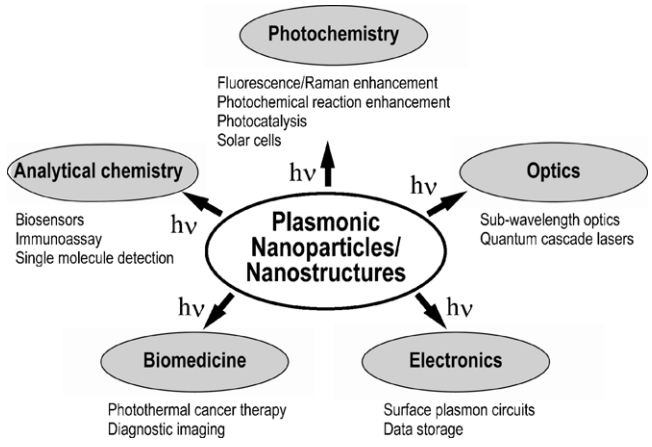

Scheme 1. Overview: the areas of current promising applications of plasmonic nanoparticles.

Photovoltaics, which is a method of converting sunlight into electricity, is a major field in photochemistry [19–21]. Approaches based on plasmonic structures can be used to improve absorption in photovoltaic devices, permitting a considerable reduction in the thickness of absorber layers and yielding new options for solar cell design [22,23]. An effect of plasmon-assisted optical antennas [24,25], where light is concentrated into a subwavelength volume to convert the incident light into amplified localized fields, has the potential to promote low-yield photochemical reactions with greater efficiency. It has been shown that two-photon-induced photochromic and photopolymerization reactions can be realized under the illumination of continuous wave (CW) lasers and halogen lamps [26–29]. Previously, these two-photon reactions have only been conducted by irradiation with high-intensity pulsed lasers. Fundamental aspects and applications of metal-enhanced fluorescence [30,31] and plasmon-assisted photocatalysts [32,33] are also active areas of research in photochemistry.

This review deals with phenomena initiated by the interaction of lasers with plasmonic NPs that give rise to rich physics and chemistry, as summarized in Scheme 2.

Briefly, the absorption of visible light by a plasmonic NP results in the instantaneous heating of the particle [34,35]. This heating has a profound effect both on the particle itself and the surrounding medium. The former can be described by electron dynamics [4–7], coherent acoustic lattice vibrations [6,36,37], melting and evaporation from the particle surface [38,39], and explosive fragmentation [40,41]. The latter is described by cavitation [42–45] and stress-wave generation [46,47], resulting from heat transfer from the particle to the surroundings. These phenomena are intriguing from a fundamental scientific viewpoint and cover a wide range of applications as will be described below (Section 4). For instance, local heating triggered by the light absorption of a plasmonic NP enables nanofabrication on particle support. The amount of heat generated by the plasmonic NP can be controlled by the particle size, shape, and aggregation state of the NP as well as the illuminating laser intensity, wavelength, and pulse duration. Thus interplay of plasmonic NPs with laser light allows spatial and temporal heat management besides the optimization of local electromagnetic field.

This review is intended to provide photochemists with information that is useful when initiating research using plasmonic NPs, in particular with lasers combined with traditional organic and inorganic photochemistry. The review focuses on metal NPs rather than semiconductor quantum dots [48,49], which are more familiar to photochemists. The photochemistry of noble metal nanoparticles is different from that of traditional molecules. Generally, the fluorescence emission of Au NPs is very weak unless the particle diameters are less than 5 nm [50]. On the other hand, Au NPs with diameters greater than 20 nm scatter light in the dark field and can be used for imaging just like fluorescent dyes or quantum dots without suffering from photobleaching/blinking [51,52]. Their particle

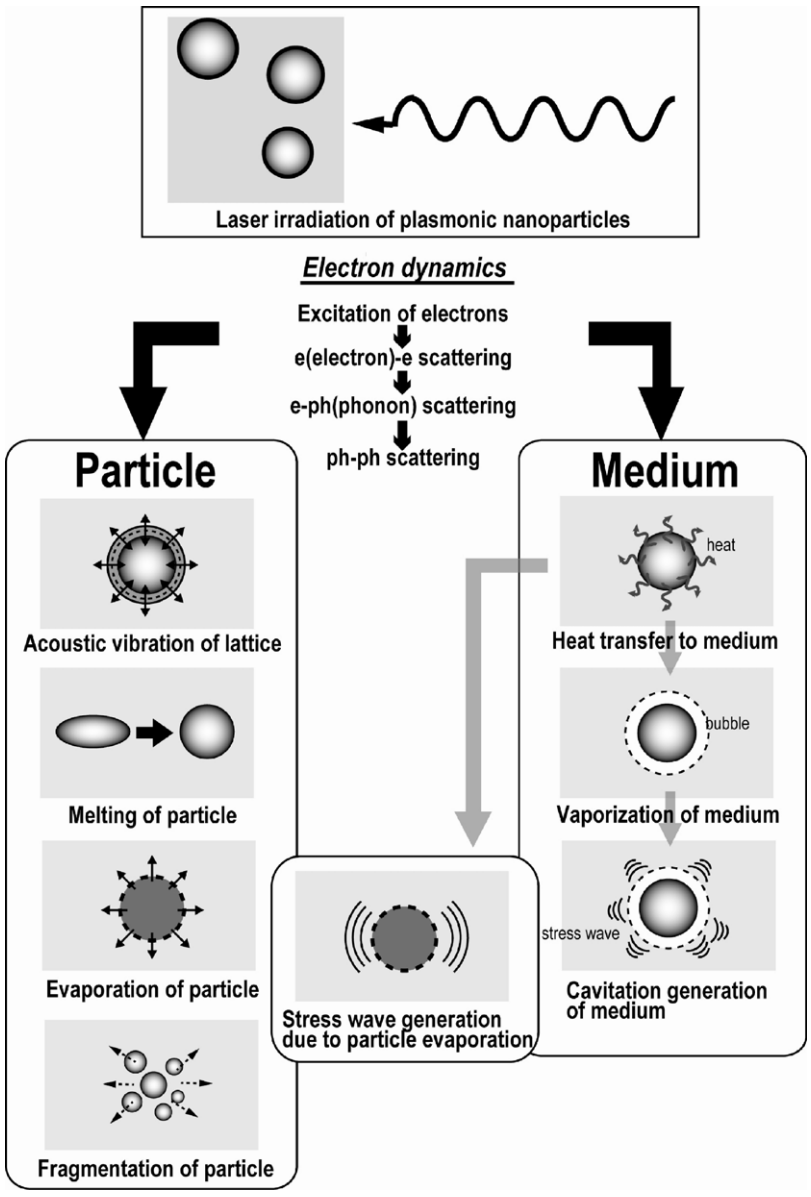

Scheme 2. Interaction of pulsed lasers with plasmonic nanoparticles and related phenomena.

size-, shape-, spacing- and medium-dependent optical properties have distinct advantages that cannot be replaced by any other materials. Note, however, that the accepted method of describing the optical properties of these metal NPs is quite different from that by which the photophysics of other molecules is delineated. This is because, for metals, frequency (wavelength)-dependent responses of dielectric functions are important. In this review, we examine the emerging field of laser–plasmonic NP interactions, leading to light manipulation, heat management, and nanofabrication. Particular emphasis is placed on Au NPs interacting with pulsed lasers. Although Ag NPs have superior characteristics in terms of plasmonic enhancement [53], Au NPs have been selected because they have higher chemical stability and are used more frequently [54,55].

2. Brief background

2.1. LSPR: localized surface plasmon resonance [1–6]

Plasmonic NPs absorb and scatter light from UV to near IR. The classical interaction of NPs with light and the resultant optical properties are described by the dielectric function ε; here ε is usually represented as a function of the angular frequency ω ($=2\pi c/\lambda$) of light. The dielectric function of gold is defined as the sum of the interband term, $\varepsilon_{IB}(\omega)$, which considers the response of 5d electrons to the 6sp conduction band, and the Drude term, $\varepsilon_D(\omega)$, which considers free conduction electrons (Drude model); thus,

$$\varepsilon(\omega) = \varepsilon_{IB}(\omega) + \varepsilon_D(\omega). \quad (1)$$

The localized surface plasmon resonance (LSPR), representing the optical properties characteristic of gold NPs, originates from the latter term, i.e. the photoexcitation of free electrons. The collective oscillation of photoexcited free electrons on the surface of Au NPs occurs via the interaction of Au nanospheres with the electromagnetic field of light, exhibiting a resonance frequency at 510–550 nm depending on the particle radius (extrinsic size effect). By contrast, the interband transition is insensitive to the particle size, yielding a threshold at 518 nm (2.4 eV). Each term of the dielectric function is divided into a real part ($\varepsilon_1(\omega) = n^2 - \kappa^2$) and an imaginary part ($\varepsilon_2(\omega) = 2n\kappa$), where n represents the refractive index and κ represents

the absorption coefficient of the metal (complex refractive index: $\overline{n} = n + i\kappa$).

Plasmonic NPs with diameters lesser than the electron-mean-free path (~40 nm for Au) allow the confinement of free electrons. According to the simplest model, the electrons are damped by a inelastic scattering process at the inner NP surface, resulting in an increased relaxation frequency or a higher damping constant Γ (s^{-1}): the relaxation time of the free-electron gas is reduced. Accordingly, the dielectric function ($\varepsilon(\omega)$) of a bulk metal has to be modified (intrinsic size effect), giving rise to a size-dependent dielectric function $\varepsilon(\omega, R)$,

$$\varepsilon(\omega, R) = \varepsilon^{\text{bulk}}(\omega) - \varepsilon_D^{\text{bulk}}(\omega) + \varepsilon_D(\omega, R) \tag{2}$$

Here $\varepsilon^{bulk}(\omega)$ describes the dielectric function of bulk metal calculated from n and κ, where values have been experimentally obtained [56]. The second term in equation (2) denotes the Drude's dielectric function of a free-electron gas defined by equation (3a), and the third term denotes the dielectric function of a NP with a radius R defined by equation (3b). Inspection of equation (2) reveals that the dielectric function of the free-electron gas $\varepsilon^{bulk}(\omega)$ determined experimentally is modified by including a size-dependent term that considers the intrinsic size effect of NPs, technically by subtracting that of the bulk metal $\varepsilon_D^{\text{bulk}}(\omega)$ and adding a modified dielectric function $\varepsilon_D(\omega,R)$:

$$\varepsilon_D^{\text{bulk}}(\omega) = 1 - \frac{\omega_p^2}{\omega^2 + i\Gamma\omega} \tag{3a}$$

$$\varepsilon_D(\omega, R) = 1 - \frac{\omega_p^2}{\omega^2 + i\Gamma(R)\omega} \tag{3b}$$

where ω_p (s^{-1}) represents the plasma frequency of the free-electron gas defined by $(n_e e^2/\varepsilon_0 m_e^*)^{1/2} = 1.38 \times 10^{16}\ s^{-1}$ for Au, where n_e is the density of the free electrons ($5.9 \times 10^{28}\ m^{-3}$ for Au), e is the electron charge (A s or C), ε_0 is the vacuum permittivity ($A^2\ s^4\ kg^{-1}\ m^{-3}$) and m_e^* is the effective mass of an electron (kg). The damping constant Γ is described by $\Gamma = v_F/l$ ($\Gamma = 1.07 \times 10^{14}\ s^{-1}$ for Au) for the bulk metal and $\Gamma(R) = v_F(1/l + A{\cdot}1/R)$ for metal nanospheres with diameters smaller than the electron-mean-free path, where v_F ($1.4 \times 10^6\ m\ s^{-1}$ for Au) is the Fermi velocity, l (3.8×10^{-8} m for Au) is the electron-mean-free path, R (m) is the NP radius, and A is a proportionality constant (A = 1 for isotropic electron scattering).

The absorption and scattering properties of spherical metal NPs are well described by applying the Mie theory [57]. The Mie theory provides exact analytical solutions to Maxwell's equations for spheres with various diameters: the absorption and scattering probabilities are represented by the absorption cross section C_{abs} (m^2), the scattering cross section C_{sca} (m^2), and the extinction cross section C_{ext}, which is the sum of both ($C_{ext} = C_{sca} + C_{abs}$). The cross section, C, of each optical event is defined by

$$I = I_0 \exp(-N \cdot C \cdot x) \tag{4}$$

where I_0 represents the intensity of incident light, I represents the intensity of transmitted light, N (m^{-3}) is the number density of particles, and x (m) is the optical pass length. Equation (4) basically expresses the Beer-Lambert law. Within the framework of the Mie theory, the absorption and scattering of light originate from free-electron oscillations driven by the oscillating electromagnetic fields of the incident light. As the diameter of the metal sphere increases, oscillations from higher orders, such as quadrupole or octapole oscillations, are likely to occur as well as the dipole mode. These oscillations are currently defined as plasmon modes. In the Mie calculation, the input parameters are the particle's dielectric function $\varepsilon_1(\omega) + i\varepsilon_2(\omega)$, radius R, and the permittivity of surrounding medium ε_m. The solution procedure is complicated, and thus not given here [58]. In the quasi-static regime where the radius R is significantly smaller than the incident wavelength λ, phase retardation and the mixing of higher-order multipole oscillations are negligible. In this case, a more simplified expression based on the dipole approximation can be used, as given by

$$C_{\text{ext}} = \frac{12\pi\omega R^3}{c_0} \frac{\varepsilon_m^{3/2}\varepsilon_2(\omega)}{[\varepsilon_1(\omega) + 2\varepsilon_m]^2 + \varepsilon_2(\omega)^2} \tag{5a}$$

$$C_{\text{sca}} = \frac{128\pi^5 R^6 \varepsilon_m^2}{3\lambda^4} \left[\frac{(\varepsilon_1(\omega) - \varepsilon_m)^2 + \varepsilon_2(\omega)^2}{(\varepsilon_1(\omega) + 2\varepsilon_m)^2 + \varepsilon_2(\omega)^2} \right] \tag{5b}$$

Here, c_0 is the velocity of light in vacuum. The resonance condition in which the peak of the LSPR band occurs is approximately fulfilled when $\varepsilon_1(\omega) = -2\varepsilon_m$, if $\varepsilon_2(\omega)$ is small or slightly dependent on ω. Note, however, that equations (5a) and (5b) cannot reproduce the size-dependent peak shift of the LSPR band because of the limitation of the dipole approximation.

Fig. 1 depicts the calculated spectra of extinction, absorption and scattering for a single spherical Au NP of various diameters. The distinct LSPR band appears at 520–580 nm. A rising shoulder with decreasing wavelengths at less than 500 nm is assigned to the interband transition. The size-dependent optical properties are very obvious. Practically, the scattering of a 20-nm Au NP is negligibly weak. A somewhat broadened spectral envelope was obtained for an extinction (absorption) spectrum owing to the intrinsic size effect. Furthermore, the LSPR band exhibits a much broader envelope for particles with much smaller than 10 nm and even disappears completely for NPs with sizes less than or equal to 2 nm. The contribution of scattering is greater with increasing diameter; for 100-nm Au particles, the relative amount of scattering cannot be ignored. Higher-order modes are more prominent with increasing particle size, causing the LSPR band to undergo a red-shift and resulting in an increased bandwidth. This is because, for large particles, the light cannot polarize the NPs homogeneously, and retardation effects lead to the excitation of higher-order modes.

The near-field scattering cross section is approximately 2 orders of magnitude greater than the scattering cross section for 20-nm Au NPs because of higher-order electric fields located on the NP surface. The fields vanish rapidly with distance. In contrast, the C_{NF} of a 100-nm-diameter Au sphere is only 1 order of magnitude greater than C_{sca}.

The experimental spectra in colloidal solutions generally agree well with the calculated spectra under the conditions of homogeneous particle size distribution and low concentrations. Besides, single-particle absorption and scattering spectra that are directly compared with the Mie theory can be measured [59,60]. Discrete dipole approximation method was performed to calculate the extinction and scattering efficiencies of non-spherical particles, rods, cubes, and triangular plates [61–63].

The LSPR band undergoes temperature-dependent spectral changes. Fig. 2 shows the extinction spectral changes of a Au NP in air on a glass substrate at various temperatures, calculated by the Mie theory using the temperature-dependent dielectric functions measured for the gold film by Otter [64]. For comparison, an experimental spectral change from literature is also shown [65].

With increasing temperature, the bleaching (intensity reduction) of the LSPR band occurs with the broadening of the spectral envelope. This can be explained by an increase in the occurrence of electron–phonon scattering at high temperatures. In this event, the reduction in the $\varepsilon_2(\omega)$ values occurs and leads to an increased damping constant Γ.

2.2. Electron dynamics, photothermal response and related phenomena

The ultrafast electron–phonon dynamics of Au and Ag NPs have been well investigated by applying femtosecond

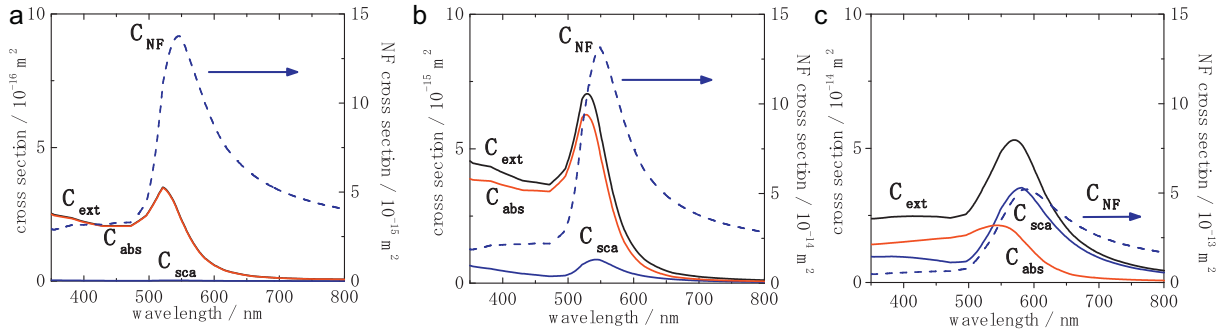

Fig. 1. Cross sections of extinction C_{ext}, absorption C_{abs}, scattering C_{sca}, and near-field scattering C_{NF}, representing scattering on the NP surface, as a function of the wavelength calculated by the Mie theory for diameters of 20 nm Au (a), 50 nm Au (b), and 100 nm Au (c) single spherical particles submerged in water (n = 1.33). Note that the ordinate scales are different: the scales in (b) are 10 times greater than those of (a) and the scales in (c) are 10 times greater than those in (b).

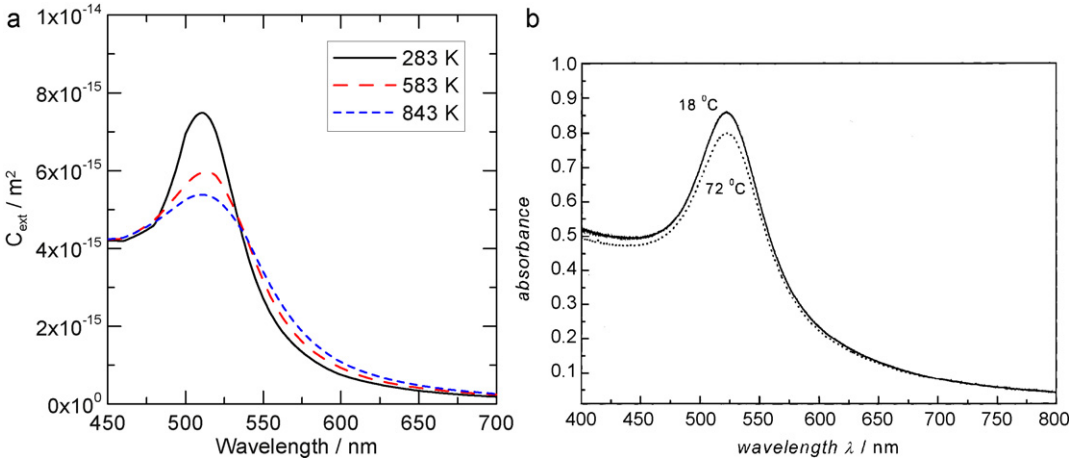

Fig. 2. (a) Computational temperature-dependent extinction spectral changes of a 60-nm Au NP placed on a glass substrate in air (effective medium refractive index: 1.1). (b) Temperature dependence of the plasmon band absorption (extinction) for the 22-nm Au NPs in water. The absorption spectra are measured at 291 K or 18 °C (solid line) and 345 K or 72 °C (dashed line). (Fig. 2b was reproduced from Ref. [65]. Reproduced with permission from the American Chemical Society.)

transient-absorption spectroscopy [66–68]. The energy deposition resulting from the laser interaction of plasmonic NPs occurs in the following four stages [35,69]. First, the laser light is absorbed by the electronic system, creating nascent nonthermal electrons. After a few 100 fs, a thermal equilibrium is reached corresponding to the Fermi distribution as a result of electron–electron scattering with cold conduction-band electrons. Subsequently, the electron energy is transferred to the NP lattice via electron–phonon coupling (<a few ps). The lattice energy is later transferred to the surrounding medium through phonon–medium interaction (<several tens to several hundreds of ps) through heating the medium at the expense of the cooling NP. The final stage is heat diffusion within the medium. Fig. 3 represents the electron relaxation dynamics of a Au NP as a function of time on excitation by a femtosecond laser [70].

The well-defined electronic temperature T_e, resulting from the internal thermalization of hot electron gas varies from hundred to several thousands of Kelvin depending on the laser pump energy and pulse duration. The lattice temperature T_L increases as a result of the energy transfer from the hot electron gas into the lattice; in the last step, the temperature of the surrounding medium T_m increases owing to the energy transfer from phonons. These consecutive processes are described well by applying the two-temperature model (TTM) [4–7,34,69–72].

The heat transfer from the NPs to the medium leads to the formation of a photothermal bubble in liquids. It is believed that heat dissipation from pulsed-laser-heated metal NPs causes an explosive evaporation of the surrounding superheated liquid, which changes into an expanding bubble formation [42,43]. Scheme 3 illustrates the process of bubble generation caused by the pulsed-laser-induced heating of a Au NP and subsequent heat dissipation to the surrounding liquid.

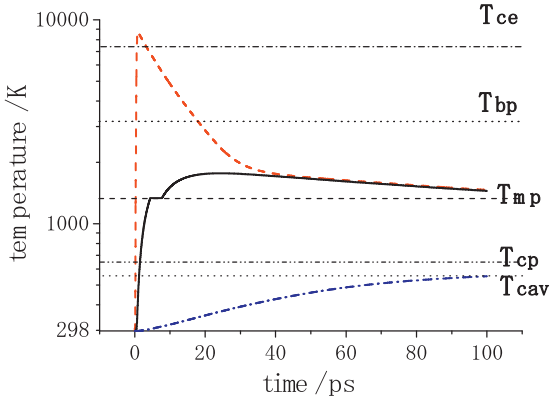

Fig. 3. Simulated temporal evolution of electron temperature T_e (dashed red curve); lattice temperature T_L (solid black curve); and maximum water temperature T_m at the NP–water interface, (dashed–dotted blue curve) for a 55-nm-diameter gold sphere absorbing a 150-fs laser pulse (full-width at half maximum; FWHM of the Gaussian time profile) at 400 nm and a laser energy density of 10 mJ cm^{-2} (P_{max} = 6.3 × 10^{10} W cm^{-2}). Horizontal lines represent temperatures at which important events occur: T_{bp}: boiling point of bulk gold (~3100 K); T_{mp}: melting point of bulk gold (1336 K); T_{cp}: the critical point of water (647 K); and T_{cav}: cavitation threshold (573 K, Ref. [73]), considering the spinodal effect of water. (Modified from Ref. [70]. Reproduced with permission from the American Chemical Society.)

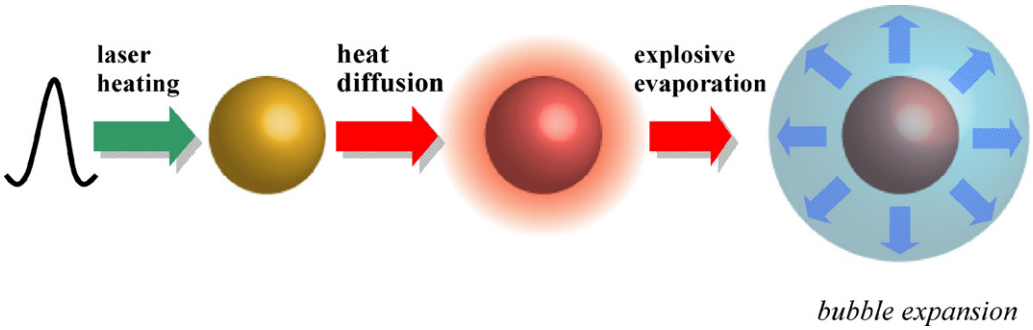

Scheme 3. Schematic illustration of explosive bubble generation in liquids through pulsed-laser-induced heating of a Au NP. The initial high-pressure shock wave caused by the fast lattice expansion of the heated NP, which passes through the water with approximately the velocity of sound, is not considered here.

2.3. Plasmonic field enhancement [74,75]

The excitation of the large optical polarization associated with LSPR results in large local electromagnetic field enhancement at the NP surface, in addition to strongly enhanced absorption and scattering by the NP at the LSPR frequency. An example for single spherical Au particles, 50, 100, and 400 nm on excitation of the LSPR band of Au is given in Fig. 4.

A greater enhancement is expected for particle diameters 40–60 nm and the optimum diameter results from both the absorption and scattering cross sections. This is clearly seen in Fig. 4, where the field enhancement of the Au NP is greater for a 50-nm-diameter particle than for 100-nm and 400-nm-diameter particles, because of the greater contribution of scattering for bigger Au NPs. The electric field is strongly localized for small spheres. Contrastingly, the dipole field of a 100-nm Au NP is distorted because of the contribution of multipole oscillations within the sphere. Further severe distortion was observed for the 400-nm Au sphere, and higher-order plasmon modes are well visible. Importantly, the intrinsic size effect (see Section 2.1) is included in the field-enhancement calculation. This is quite important, if the Au NP radius is less than or equal to the electron-mean-free path. For instance, by neglecting the intrinsic size effect, the electric field-enhancement factor increases to 6.04 for 50-nm Au NPs. The difference is more dramatically observed for 20-nm-diameter Au NPs, where the field-enhancement factors are 4.58 with the intrinsic size effect and 5.36 without it. Greater field enhancement was postulated on the basis of experimental studies for non-spherical particles and nanostructures, including nanorods [76] and triangles [77] with sharp edges, for which field calculations on the basis of finite-difference-time-domain (FDTD) simulations supporting the observations were given [75–79].

The near-field scattering efficiency, defined by $Q_{NF} = C_{NF}/\pi R^2$, is a measure of the ability of a sphere to extract power from the incident wave and redirect it as scattering power over the whole surface. Q_{NF} is considerably greater than unity. This implies that the influence of the sphere on the incident light extends beyond its geometrical boundaries. In other words, a spherical Au NP can act as a field amplifier. Q_{NF} is an important parameter for surface-enhanced Raman scattering (SERS). Fig. 5a shows Q_{NF} as a function of the diameter of Au NPs surrounded by water, calculated both at 532 nm and at the peak positions of the C_{NF}.

When excited at 532 nm, the value of Q_{NF} increases with increasing NP diameter, reaching a plateau at diameters between 50 and 60 nm. This behavior can be explained by a greater increase in the dependence of scattering cross section on the NP size because of the reduced contribution of the intrinsic size effect. Further increase in diameter leads to a reduced near-field scattering efficiency because the field retardation and geometrical cross section start to dominate. By contrast, the curve given by the peak position of Q_{NF} is shifted to larger NP sizes. This is reasonable because a red-shift occurs for the resonance wavelength of the C_{NF}. For instance, the wavelength at the maximum peak position of C_{NF} is 549 nm for a 50-nm-diameter Au NP and 587 nm for a 100-nm Au NP. The near-field scattering efficiency can be significantly larger than the scattering efficiency Q_{sca}, which is a measure of the far-field scattering. This is because Q_{NF} involves fields that increase more rapidly than the dependence of $1/a$ (a is the distance from the surface of a metallic sphere) as one moves from the far field to the surface of the sphere. Thus, the integrated near-field intensity includes additional field components that appear only in the near-field region. Fig. 5b gives the values of Q_{NF} as a function of a for a 50-nm Au NP dispersed in water. The figure shows that Q_{NF} decays very quickly within a distance of 25 nm, where Q_{NF} decreases to 7.8% of the maximum value. After a distance of 50 nm is reached, Q_{NF} is only 2.1% of the surface value. This value is nearly equal to Q_{sca}. At this distance, the far-field effect dominates.

3. Photo-induced dynamics of metallic nanoparticles

3.1. Shape transformation

Pulsed-laser irradiation of Au nanorods suspended in water resulted in a shape change to spherical particles [38,39,80–82]. The shape transition of the nanorods was studied by Chang et al. [80] by exposure to 532- and 1064-nm nanosecond (6 ns) lasers. They ascribed the observed rod-to-sphere conversions to a photoannealing process. Link and co-workers carried out a similar experiment by applying both femtosecond (800 nm, 100 fs) and nanosecond (355 nm, 7 ns) lasers [38,39,81]. They observed that both lasers basically contribute to the photothermal reshaping of Au nanorods in an aqueous solution. They also found that femtosecond lasers are better suited for reshaping purpose because the energy threshold for complete melting of the nanorods is reduced by a factor of 100 when using the femtosecond laser. This is because femtosecond lasers have such a high intensity that the rate of absorption, and thus heating the lattice, is extremely rapid. This point will be described later with reference to temperature simulation.

Zijlstra et al. [82] observed a gradual shape change from a long and thin rod to a shorter and wider rod, which eventually collapsed into a sphere, thus ambiguously confirming the assumption of the rod-to-sphere transformation actually occurring (Fig. 6). In this case, a simple calculation showed that the mp of gold (1337 K) is attained for the complete transformation by the laser energy deposited (260 fJ or 2.1 mJ cm^{-2}) for nanorods with dimensions 92 × 30 nm under the condition of negligible heat dissipation.

It has been known that NPs exhibit a melting temperature that depends on particle size because of the effect of the surface-to-volume ratio. A remarkable decrease in the melting temperature was observed for particle diameters less than 5 nm [83–85]. For

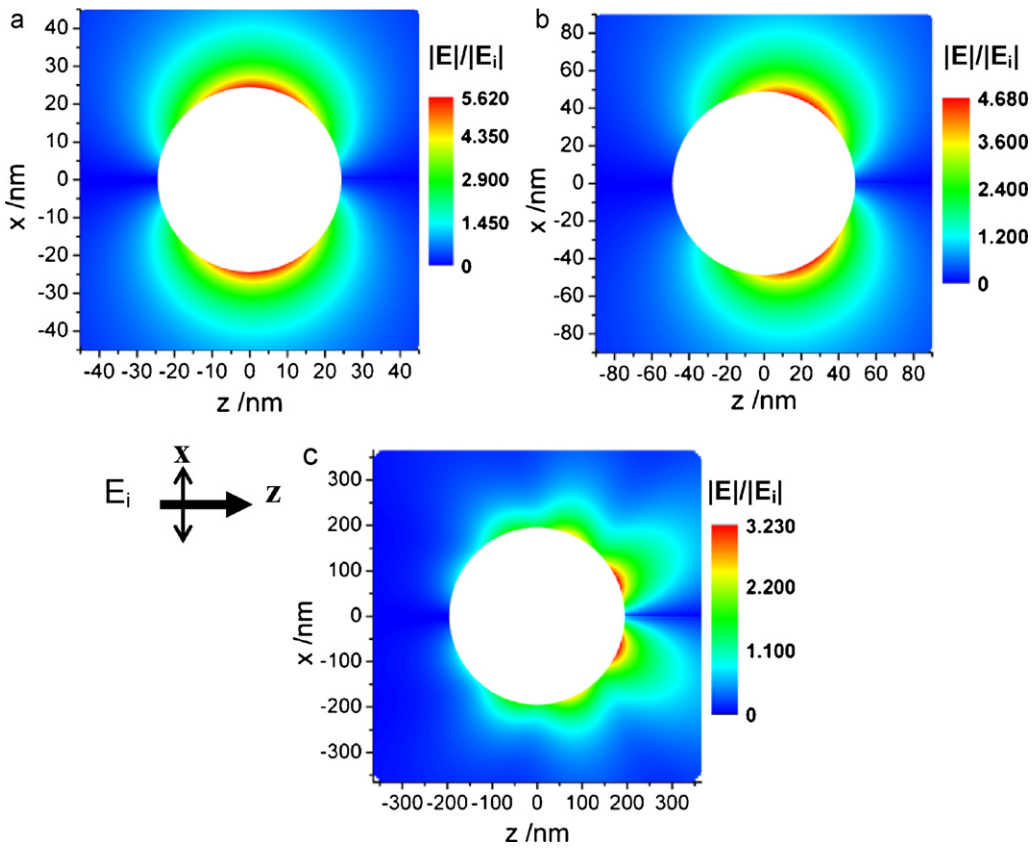

Fig. 4. Electric field ($|E|/|E_i|$) distributions for diameters of 50 nm (a), 100 nm (b), and 400 nm (c) Au spheres submerged in water ($n = 1.33$) on excitation by a plane-polarized light with a wavelength of 532 nm. The calculation was performed on the basis of the Mie theory. The *k*-vector of the incident field E_i is collinear in the *z*-direction and the electric field oscillates in the *x*–*z* plane. The field in the *y*–*z* plane was not given because of insignificant enhancement. Note that the light intensity is the square of the field strength, and thus, the enhancement of incident light intensity should be $(|E|/|E_i|)^2$.

particles lesser than 5 nm, the homogeneous melting temperature is inversely proportional to the radius of the particle, whereas for larger particles, melting occurs near the mp of bulk gold. Experimentally, the melting temperature of a 38-nm Au NP has been found to be ~1067 K (~830 °C), which is 200 K lesser than that of bulk gold with a mp of 1337 K (1064 °C) [86]. Distinct from the entire particle melting at above the melting temperature, it was demonstrated that shape changes induced by surface melting occur at temperatures much lower than the mp of bulk gold. For instance, a transformation in the shape of average 38-nm elliptical Au NPs resulting from surface melting was observed at temperatures as low as 673 K (400 °C) when the particles deposited on a silicon substrate were heated in a muffle furnace and inspected using SEM [86]. Thermal heating experiments affirmed that a temperature of 523 K (250 °C) is sufficient to completely transform nanorods into spheres within an hour [87]. In this case, reshaping was observed even at 373 K (100 °C). A phase transformation ascribable to the formation of a core–shell structure of a particle with a surface melting layer was experimentally observed at 377 K (104 °C) [88]. These results suggest that surface melting occurs at a temperature much lower than the mp of bulk gold.

Pulsed-X-ray scattering was used to examine the lattice expansion and melting dynamics in Au NPs (100-nm diameter) in water, following excitation with femtosecond-laser pulses (excitation wavelength: 400 nm) [89]. At the excitation power corresponding to temperatures below the mp of bulk gold, the lattice shows

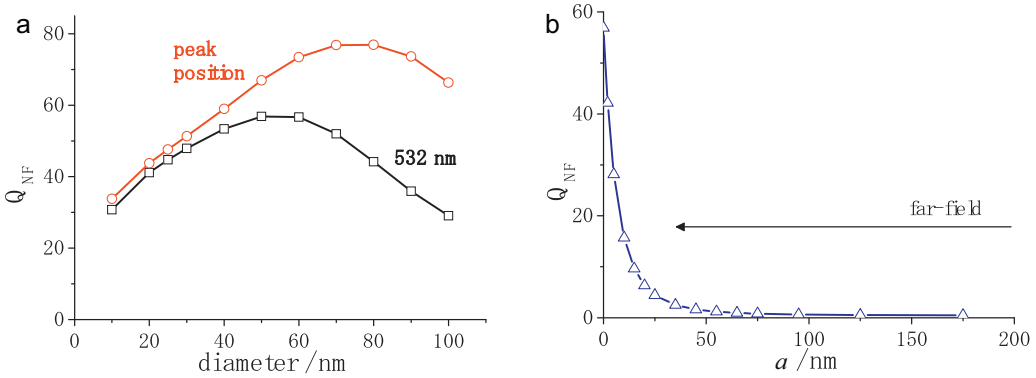

Fig. 5. (a) Near-field scattering efficiency Q_{NF} as a function of the diameter of Au NP surrounded by water, calculated both at 532 nm and at the peak positions of the C_{NF}; (b) Q_{NF} as a function of *a* (the distance from the surface of a metallic sphere) for a 50-nm Au NP dispersed in water.

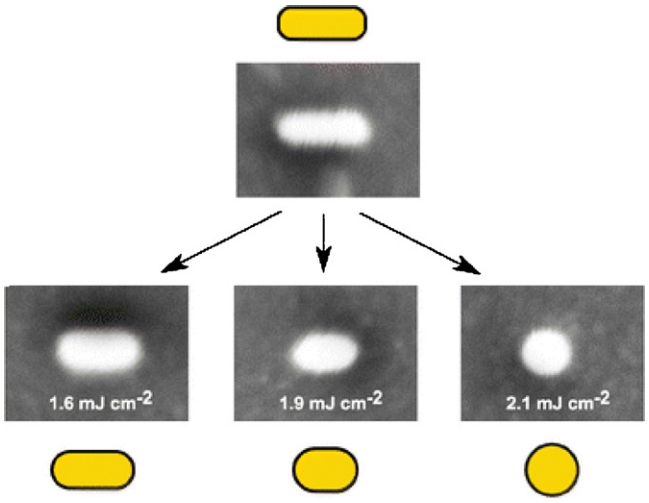

Fig. 6. Sketch of the intermediate particle shapes observed at different pulse-energy densities. The dimensions of all scanning electron microscopy (SEM) images are 200 × 150 nm. The laser irradiation was conducted by a single pulse of 100 fs duration with a wavelength of 800 nm. (Reproduced from ref. 82. Reproduced by permission of the PCCP Owners Society.)

a loss of long-range order owing to the premelting of the particle. When the power was increased to the melting temperature of bulk gold, complete melting occurred within 100 ps after laser excitation. Because of the limitation of the time resolution of the system, the detection of earlier events was not possible. Besides, one would have to differentiate between particle melting of the particle ensemble and that of the structure of each single particle.

3.2. Fragmentation and size reduction of gold nanoparticles

3.2.1. Possible mechanism of size reduction

Exposure of Au and Ag NPs to a single-shot laser or a number of shots of pulsed lasers allowed the size reduction or fragmentation [38,39,70,90–100]. The laser-induced size reduction has attracted significant attention from researchers in the related fields. This phenomenon includes the fundamental aspects of interplay between NPs and lasers such as how photon energy flows within NPs, leading to the destructive event, and how fast the energy flow occurs. In addition, the method can be utilized for controlling particle size and the size distribution in the laser-ablation-based nanoparticle generation [101–105]. Three types of mechanisms have been known to consider size reduction, as illustrated in Scheme 4 [70].

Koda and co-workers [90] proposed a heating–melting–evaporation concept (Scheme 4 (1)) for the observation of the size reduction of chemically prepared aqueous Au NPs with sizes ranging from 19 to 47 nm diameter. In their experiments, the LSPR band was exposed to various intensities and numbers of a 532-nm nanosecond-pulsed-laser beam. Assuming negligible heat transfer to the surrounding water, they considered that the size reduction starts to occur when the particle temperature exceeds the boiling point of bulk gold. The calculation of the particle temperature T (K) was performed by applying simple thermodynamics:

$$T[K] = \frac{Q - \Delta H_{\mathrm{melt}} - \Delta H_{\mathrm{vap}}}{C_p} + 293 \quad (6)$$

Here Q (J g^{-1}) represents the energy absorbed by a unit mass of gold by the irradiation of a single pulsed-laser light, C_p is the specific heat capacity of Au, 0.131 (J g^{-1} K^{-1}) and ΔH_{melt} is the enthalpy of melting, 6.28×10^1 (J g^{-1}), and ΔH_{vap} is the enthalpy of vaporization, 1.87×10^3 (J g^{-1}). In support of the photothermal mechanism, Inasawa et al. [91] conducted further detailed research through the use of a 355-nm picosecond laser. They revealed that the size reduction of Au NPs takes place by a layer-by-layer mechanism based on the observation of the bimodal distribution of particle sizes that are slightly smaller and much smaller than the original ones. They concluded that the irradiation by picosecond-laser pulses is the most efficient way to induce the size reduction of Au NPs. Later, Pyatenko et al. [92] carried out a calculation to examine the melting and size reduction of gold NPs and concluded that the photothermal mechanism prevails at low laser intensities. He also concluded that the excitation of the LSPR band of Au NP by a 532-nm nanosecond laser is more efficient because of a greater absorption cross section C_{abs}, compared with other wavelengths, such as 1064 and 355 nm, but gave no experimental evidence. Werner et al. carried out the measurement of the dependence of the size-reduction threshold on the excitation wavelength [93]. They found that the interband excitation is more efficient than the LSPR excitation.

In contrast to the photothermal evaporation concept, a Coulomb explosion model is given in Scheme 4 (2). The Coulomb explosion model presumes the ejection of quite a large number of electrons to generate multiple ionized NPs that undergo spontaneous fission because of the charge repulsion. Kamat et al. adopted this model to interpret the 355-nm picosecond-laser-induced splitting of Ag NPs, because they detected hydrated electrons in the transient-absorption measurement [94]. Subsequently, Mafune and co-workers observed hydrated electrons on intense nanosecond-pulsed-laser excitation of Au NPs in aqueous sodium dodecyl sulfate (SDS) [95,96]. Their results indicated higher size-reduction efficiencies for 355-nm irradiation than for the excitation of the LSPR band of the gold NPs. The observed high efficiency was explained by interband electronic excitation–relaxation cycles that enable a faster absorption of a new photon than the conduction-band electrons can absorb. Furthermore, they detected positively charged Au ions by applying mass spectrometry and proposed that thermionic emission of electrons due to the interband excitation is responsible for the highly efficient splitting of Au NPs [97,98]. More recently, Giammanco et al. developed a theoretical analysis based on the TTM to explain the fragmentation of gold NPs by picosecond-laser irradiation [99]. They excited rather small gold NPs with an average diameter of 3.5 nm stabilized with poly(amidoamine) PAMAM-G5 in water. By fitting their experimental data with the theoretical analysis, they concluded that the evaporation of the NPs does not play a relevant role in comparison to the Coulomb explosion resulting from thermionic electron emission and photoelectric effect. However, they did not consider the depletion of mp and bp and the quantum confinement effect for such small particles.

The photothermal and Coulomb explosion mechanisms have been investigated independently and no unified concepts have been developed to distinguish the two mechanisms. For instance, it remained unclear under what conditions of pulse width and laser energy one mechanism surpasses the other. In the Coulomb explosion mechanism, the electron dynamics that govern various relaxation processes including electron emission, play a major role in electronic excitation. In contrast, in the photothermal evaporation mechanism, evaporation from the particle surface plays a major role. In this case, the thermal energy deposited into the lattice system results in the heating of NPs to the evaporation point depending on the evaporation pressure of the material. Until recently, precise theoretical calculations to determine the thresholds for surface evaporation and Coulomb explosion have been unavailable, especially for the nanosecond-pulsed-laser excitation of NPs. Table 1 summarizes the previous studies of pulsed-laser-induced size reduction. Not many studies gave the experimental threshold of size reduction. The threshold is so important to identify the precise mechanism.

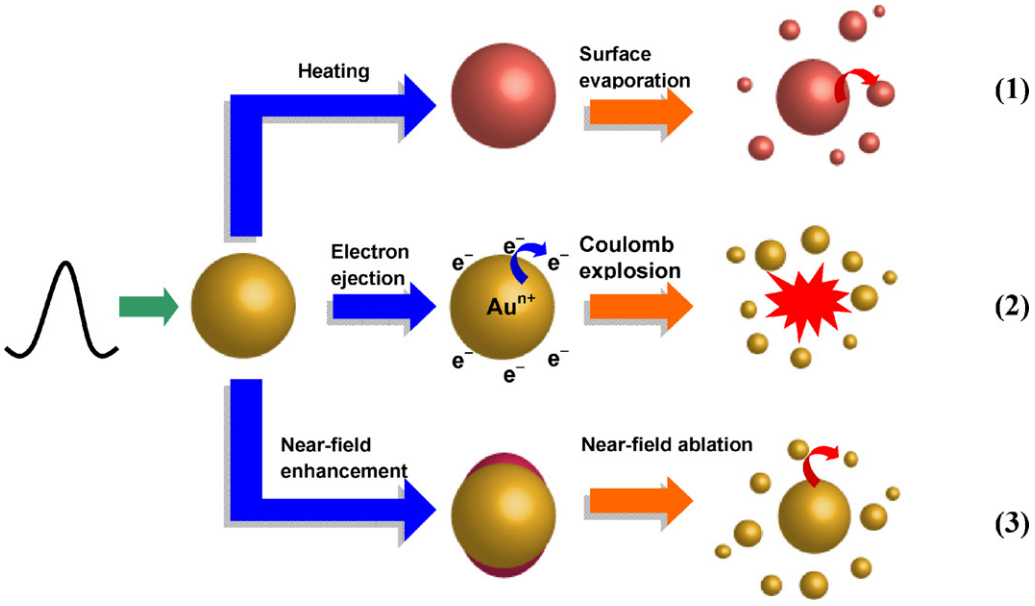

Scheme 4. Schematic illustration of size reduction and fragmentation mechanisms of plasmonic NPs in a colloidal solution.

In addition to the photothermal evaporation and Coulomb explosion mechanisms, a near-field ablation mechanism [106] has been postulated exclusively for extremely high-intensity femtosecond-laser excitation (Scheme 4 (3)). The mechanism assumes that the spallation of solid Au NPs takes place by the action of an intense laser field that was caused by the plasmonic near-field enhancement. The experimental proof for the mechanism is still not convincing because of the following reason. The near-field ablation of Au NPs in water is supposed to take place well before the melting of the nanorods (NRs). However, El-Sayed's group [81] and Zijlstra et al. [82] have shown that Au NRs can easily melt to form spherical NPs (see Section 3.1) without undergoing fragmentation. Au NRs have a much higher field-enhancement factor (see Section 2.3) than spherical NPs. This may cause near-field ion emission leading to the Coulomb explosion at much lower laser densities than those observed by Plech's group [106]. Thus the concept of near-field ablation contradicts the observations of melting without fragmentation. Werner's group performed field-intensity calculations on the surface of 60-nm Au NPs in water and concluded that the field strength at the fragmentation threshold is not sufficiently high for ion emission [70].

3.2.2. Temperature calculation to elucidate the mechanism

Werner and Hashimoto [100] conducted a precise calculation of time-dependent temperature profiles to elucidate the size-reduction mechanism of aqueous colloidal Au NPs, which is dependent on excitation laser-pulse duration (femto-, pico- and nanosecond), excitation laser energy, and excitation laser wavelength. They conducted a simulation based on both a TTM [4–7,34,71,72,107–110] describing electron-lattice heating and the liquid-droplet model of fragmentation [111,112] to distinguish the Coulomb explosion mechanism from photothermal surface evaporation. Here three temperatures were considered: electron temperature T_e, lattice temperature T_L, and the temperature of the medium surrounding the particle T_m.

$$C_e(T_e)\frac{dT_e(t)}{dt} = -g(T_e)\cdot(T_e - T_L) + S(t) \tag{7a}$$

$$C_L(T_L)\frac{dT_L(t)}{dt} = g(T_e)\cdot(T_e - T_L) - F \tag{7b}$$

$$C_m(T_m)\frac{\partial T_m(r,t)}{\partial t} = \frac{1}{r^2}\frac{\partial}{\partial r}\left(k_m r^2 \frac{\partial T_m(r,t)}{\partial r}\right) + F \tag{7c}$$

Table 1
Threshold laser power densities taken from available literature.

Target particle (diameter)	Pulse duration	Excitation wavelength	Threshold energy[a]	Mechanism[b]	Threshold peak power	Year	Source
Au sphere (19–47 nm)	7 ns	532 nm	40–50 mJ cm^{-2}	PT	6–7 MW cm^{-2}	1999	[90]
Au sphere (25 ± 8 nm)	30 ps	355 nm	17 mJ cm^{-2}	PT	560 MW cm^{-2}	2005	[91]
Au sphere (10–100 nm)	10 ns	355 nm	NA	PT	300 MW cm^{-2}	2009	[92]
Au sphere (10–100 nm)	10 ns	532 nm	NA	PT	150 MW cm^{-2}	2009	[92]
Au sphere (10–100 nm)	10 ns	1064 nm	NA	PT		2009	[92]
Au sphere (55 ± 7 nm)	4–6 ns	266 nm	20 mJ cm^{-2}	PT	3.8 MW cm^{-2}	2011	[100]
Au sphere (55 ± 7 nm)	4–6 ns	355 nm	24 mJ cm^{-2}	PT	4.5 MW cm^{-2}	2011	[100]
Au sphere (55 ± 7 nm)	4–6 ns	532 nm	33 mJ cm^{-2}	PT	6.2 MW cm^{-2}	2011	[100]
Ag sphere (40–60 nm)	18 ps	355 nm	NA	CE		1998	[94]
Au sphere (10 nm)	10 ns	355 nm	NA	CE	27 GW cm^{-2}	2007	[96]
Au sphere (3.5 nm)	15 ps	355 nm	NA	CE	1.2 GW cm^{-2}	2010	[99]
Au sphere (3.5 nm)	20 ps	532 nm	NA	CE	0.5 GW cm^{-2}	2010	[99]
Au sphere (60 ± 8 nm)	150 fs	400 nm	7.3 mJ cm^{-2}	CE	46 GW cm^{-2}	2011	[70]
Au sphere (60 ± 8 nm)	150 fs	532 nm	3.6 mJ cm^{-2}	CE	23 GW cm^{-2}	2011	[70]
Au sphere (38 nm)	100 fs	400 nm	9–12 mJ cm^{-2}	NF	90 GW cm^{-2}	2006	[106]
Au sphere (80 nm)	~6 ns	355 nm	120 mJ cm^{-2}		20 MW cm^{-2}	2007	[118]

[a] NA: not available.
[b] PT: photothermal evaporation; CE: Coulomb explosion; NF: near-field ablation.

Equation (7a) describes the evolution of the electron temperature T_e coupling to the lattice with the electron–phonon coupling constant of $g(T_e)$, and the laser irradiation term $S(t)$. Equation (7b) describes the dynamics of the lattice temperature T_L that include heat transfer across the interface between the particle and its surroundings, expressed by a term F. Finally, equation (7c) describes the medium temperature on a spherical surface dependent both on the time and distance from the particle center r. Here $C_e(T_e)$, $C_L(T_L)$, and $C_m(T_m)$ are the electron, lattice, and medium specific heat capacities, and k_m is the thermal conductivity of medium. $S(t)$ and F are given by

$$S(t) = \frac{C_{\text{abs}}^{\lambda}(n_m, R) \cdot P(t)}{V_p(T_L)} \tag{8}$$

$$F = \frac{h \cdot A_P}{V_P}[T_L - T_m(R)] \tag{9}$$

Equation (8) shows that the energy absorption by laser irradiation is described by the absorption cross section C_{abs} (m^2) multiplied by the laser power density, P (J m^{-2}) and divided by the particle volume V_p (m^3). Most importantly, $S(t)$ represents energy truly absorbed by a NP irradiated with a laser energy density of P. In equation (9), h (a typical value is 100 $\text{MW m}^{-2}\,\text{K}^{-1}$ for 100-nm Au NPs in water [89]) is the interface thermal conductance, A_p (m^2) is the particle surface area, and $T_m(R)$ is the maximum water temperature at the NP–water interface. Note that, in equations (8) and (9), R denotes the particle radius.

The simulation model, which is based on a previous thermophysical calculation of Au nanorods on the excitation by femtosecond-laser pulses [69], can be improved, especially for ultrashort pulse heating of Au NPs by taking advantage of a previous theoretical treatment [113]. An exhaustive description of the electron heat capacity and the electron–phonon coupling factor was complied by applying the real electron density of states, Fermi distribution, and temperature-dependent chemical potential. It has been revealed that the free-electron gas model (FEG) with its linear temperature-dependent electron heat capacity ($C_e(T_e) = \gamma T_e$), assuming a parabolic electron density of states and a constant electron–phonon coupling factor, is valid only at temperatures below the electron temperature of 2500 K [113]. Above 2500 K, the real electron heat capacity differs significantly from that of the FEG model. For instance, at 10,000 K, the electron heat capacity of gold is three times higher than that derived from the FEG model. Importantly, this high electron temperature can be easily attained via femtosecond-laser excitation. For instance, Fig. 7a shows the simulation results of temperature evolution based on the FEG model. Here exactly the same laser parameters were used as those used in the rigorous model that leads to the computational result given in Fig. 3 for 55-nm aqueous Au NP colloids.

A comparison of Figs. 3 and 7 may deserve attention. Significantly overestimated T_e values were obtained in the initial stage when the FEG model was used (Fig. 7a). However, the values of T_L at 60–100 ps delays in Fig. 7a are similar to those observed in Fig. 3, suggesting that the estimation of T_L is still acceptable for the calculation based on the FEG model. Fig. 7b gives the temperature profile when the heat dissipation to the surrounding water is intentionally neglected. Fig. 7b shows that heat losses can be neglected to obtain T_L in the femtosecond-pulse excitation with reasonable accuracy because of the slow heating process of the surrounding water. This explains why the heat dissipation was negligible in the temperature calculation of Au nanorods excited by a femtosecond laser [82]. The limited applicability of the FEG model was observed for the electron–phonon coupling factor [113]. Werner's group adopted temperature-dependent density changes of the nanoparticle and water and a Gaussian time profile of a laser pulse in $S(t)$ [100]. These points were important in estimating the temperature dynamics but were not considered previously [69].

According to the investigation by Werner's group [100], the Coulomb explosion mechanism operates if the electron temperature exceeds a certain threshold. This is because, at high T_e such as 5000 K, sufficiently energetic electrons in the tail of the Fermi distribution can overcome the work function of a metal and escape from the surface. This process is known as thermionic electron emission [97,98]. The probability of electrons thermionically emissible from one atom can be calculated by

$$n_\varepsilon = \int_{\varepsilon}^{\infty} \text{EDOS}(E) f(E, \mu(T_e), T_e)\, dE \tag{10}$$

where EDOS(E) is the electron density of states, f is the Fermi distribution defined as $f = (\exp[(E-\mu)/k_B T_e] + 1)^{-1}$ dependent on the chemical potential μ, and T_e. The fission probability depends on the ratio of the Coulomb expulsion term to the surface energy of a particle: if the former exceeds the latter, charged droplets are unstable to undergo explosion, which has been known since the pioneering study by Rayleigh (Rayleigh instability) [114,115]. The fragmentation temperature T_e (frag), at which the electron temperature exceeds the threshold to emit a sufficient number of electrons to cause instability, can be obtained. For instance, for a 60-nm-diameter Au NP, T_e (frag) can be calculated as 7300 K in the liquid state, and as 8200 K in the solid state. At 7300 K, the number of electrons ejected is calculated as 600, and at 8200 K, it is 1500. Obviously, the liquid NP is less stable than the solid because of the reduced surface energy.

The temperature calculation in the nanosecond regime is more simply performed because the electron–phonon coupling is completed in the nanosecond-time domain. Thus, equation (7a)–(7c) reduces to a set of equations given in the following (one-temperature model (OTM)) [116]

$$C_L(T_L)\frac{dT_L(t)}{dt} = -F + S(t) \tag{11a}$$

$$C_m(T_m)\frac{\partial T_m(r,t)}{\partial t} = \frac{1}{r^2}\frac{\partial}{\partial r}\left(k_m r^2 \frac{\partial T_m(r,t)}{\partial r}\right) + F \tag{11b}$$

Fig. 8 shows temperature versus time curves obtained by a simulation using equation (11a) and (11b) for the nanosecond-laser excitation.

Two different laser power densities were employed in the simulation. The increase in particle temperature (or lattice temperature T_L) takes place monotonously with time, passing through the mp of bulk gold and reaching the bp of bulk gold, in both Fig. 8a and b. At much higher laser power densities, however, a much rapid temperature increase is noted, as shown in Fig. 8b. Note that even with the simulation using the TTM given in equation (7a)–(7c), the time profiles of T_e and T_L obtained are quite similar to those of the OTM. This suggests that as long as nanosecond-laser pulse is used, no mechanistic difference can be expected between the TTM and OTM. The simulation also suggests that bubble formation can take place during the nanosecond-laser pulse duration because of the explosive evaporation of water, superheated well above the bp of water up to the critical temperature (647 K). The formation of a bubble around a NP presumably induces the reduction in the refractive index from 1.33 to 1.0. As a result, a significant reduction in the optical absorption of Au NP can result, as depicted in Fig. 9. The thermal insulation of NPs within the bubble is also expected.

Importantly, the absorption cross section (C_{abs}), which determines the absorbed laser power in equation (8), largely depends on the temperature-dependent optical properties of both the Au NP and the surrounding medium. In the femtosecond-pulsed-laser excitation regime, where the pulse duration is smaller than the

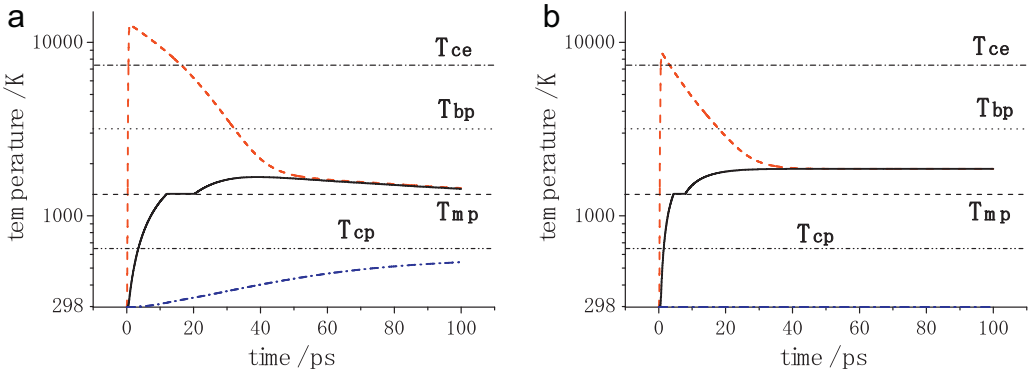

Fig. 7. Time-dependent temperature profiles of electron temperature T_e (dotted curve), lattice temperature T_L (solid curve), and the temperature of the medium surrounding the particle T_m (dashed dotted curve), calculated for the 55-nm-diameter Au sphere by applying the FEG model (a) and the evaluation of T_e and T_L calculated when heat dissipation to the surrounding water was neglected (b). Exactly the same laser parameters as those given in Fig. 3 were used.

electron–electron and electron–phonon relaxation time scales, C_{abs} can be calculated with the optical properties at ambient temperature C_{abs} ($n_m(T_{ambient})$, R). Here the pulse energy is totally absorbed by the NP before the temperatures of the electrons, lattice, and surrounding medium increase significantly. On the other hand, in the nanosecond-pulsed-laser excitation regime, T_e, T_L, and T_m increase simultaneously during the Gaussian pulse-time profile. Thus, C_{abs} is dependent on temperature, assuming the following very complex form: $C_{abs}(n_m(T_m, p), R, T_L, R_B)$. Here the medium refractive index n_m is a function of the temperature and pressure gradients around the Au NP. If T_m exceeds the threshold of nanobubble formation, the refractive index in the vicinity of the Au NP decreases to a minimum value of 1.00, and the value of C_{abs} is significantly reduced inside the expanding bubble with a radius of R_B. Furthermore, lattice heating induces the changes in the optical properties of the Au NPs, which have been mentioned above (see Fig. 2). All these points make the temperature calculations in the nanosecond-excitation regime very difficult because of insufficient knowledge about the behavior of the nanobubble expansion and collapse. However, it should be pointed out that without considering of this bubble effect, an accurate estimation of the size-reduction threshold is not possible.

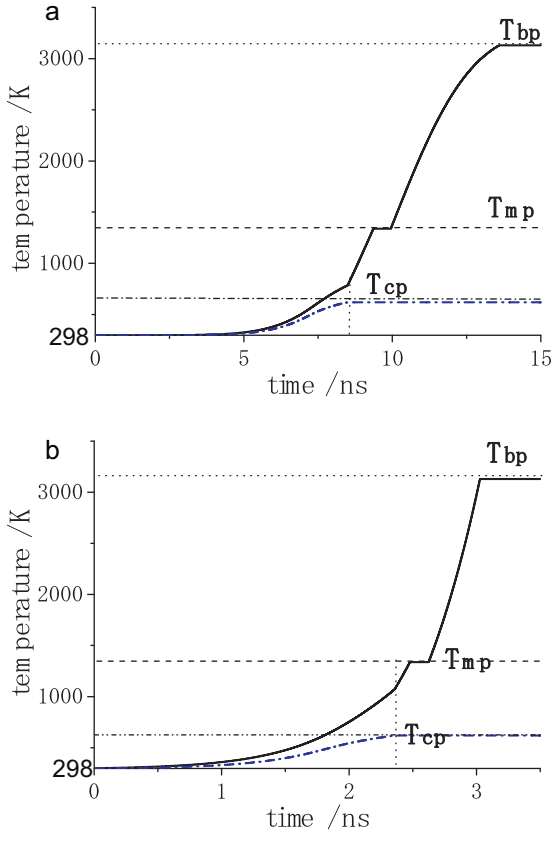

Fig. 8. Temperature versus time curves for lattice (particle) temperature T_L (solid curve) and maximum water temperature T_m at the NP–water interface (dashed–dotted curve) for a 55-nm-diameter Au particle interacting with a 5-ns laser pulse (FWHM of the Gaussian time profile) at 355 nm, 28 mJ cm^{-2} ($P_{max} = 5.26 \times 10^6$ W cm^{-2}) (a) and 52 J cm^{-2} ($P_{max} = 9.77 \times 10^9$ W cm^{-2}) (b). See the caption of Fig. 3 for symbols T_{bp}, T_{mp}, T_{cp}. (Modified from ref. 100. Reproduced with permission from the American Chemical Society.)

3.2.3. *Interpretation of experimental size reduction based on temperature simulation*

The experimental study of size reduction can be demonstrated by in situ absorption (extinction) spectroscopy assisted by transmission electron microscopy (TEM). Fig. 10a shows an example of in situ spectral changes recorded for the size-reduction experiment of the 60-nm-diameter Au NP excited by a femtosecond laser with a wavelength at 400 nm. Fig. 10b shows the plots of experimental ΔA, the changes in LSPR band peak intensity, after 3,600,000 shots (1 kHz, 60 min) as a function of the laser power density (scale on the left) on excitation at 400 nm.

In Fig. 10b, a slightly decreased ΔA occurs at a laser power density of 2.5 mJ cm^{-2} and ΔA remains constant up to 5.0 mJ cm^{-2}. When the laser power density increases to 7.3 mJ cm^{-2}, a greater

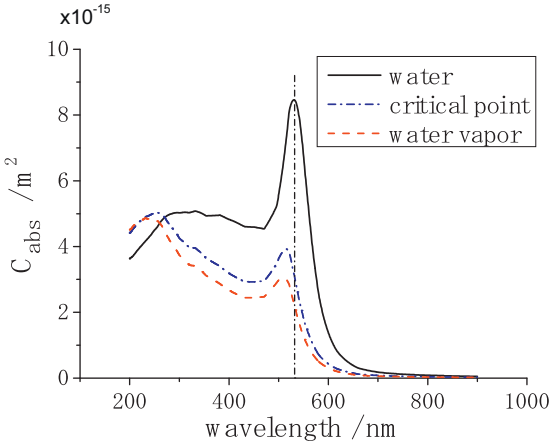

Fig. 9. Absorption cross section curves as a function of wavelength for a 55-nm-diameter Au NP in water of various phases: liquid ($n = 1.33$), critical state ($n = 1.07$), and vapor ($n = 1.00$). (Reproduced from ref. [100]. Reproduced with permission from the American Chemical Society.)

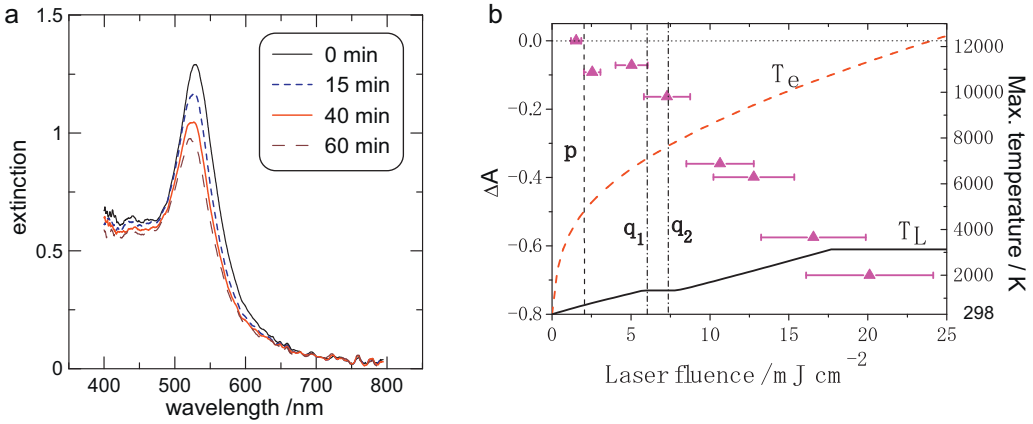

Fig. 10. (a) Typical time sequence of in situ spectra for 60-nm Au NPs in aqueous solution during femtosecond-pulsed-laser irradiation at 400 nm, and a laser power density of 19.4 mJ cm^{-2}. The spectra were recorded at 0, 15, 40, and 60 min. The repetition rate was 100 Hz. (b) Plots of experimental ΔA, the change in the LSPR band peak intensity after 3,600,000 shots (1 kHz, 60 min) as a function of laser power density (scale on the left) on excitation at 400 nm by a femtosecond laser (150 fs). Calculated laser power density dependent maximum temperature evolution of T_e (dashed red line) and T_L (solid black line) for a 60-nm aqueous Au NP (scale on the right) is also included. The vertical dashed-dotted lines (q_1 = 6.0, q_2 = 7.4 mJ cm^{-2}) indicate the range of the calculated Coulomb explosion threshold for liquid gold nanodroplets. The dashed line shows the reshaping threshold at 700 K. (Reproduced from [70]. Reproduced with permission from the American Chemical Society.)

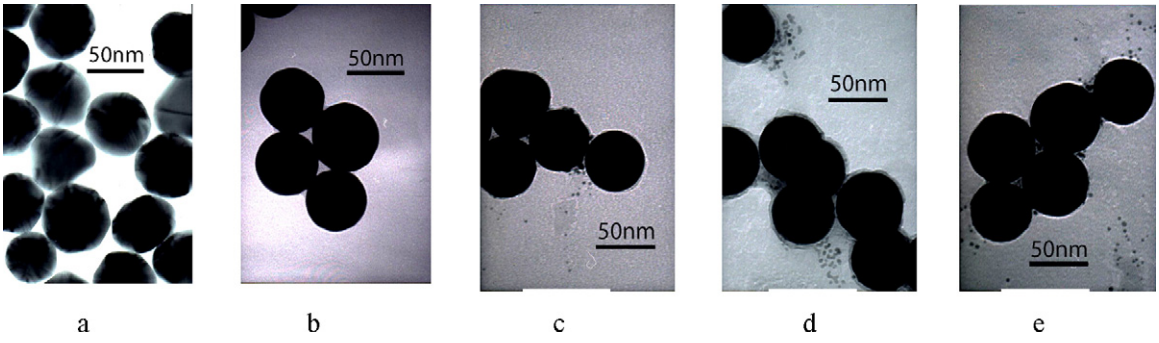

Fig. 11. TEM images of 60-nm Au NPs after 60 min of femtosecond-laser irradiation at 100 Hz at an excitation wavelength of 400 nm, (a): 0 mJ cm^{-2}, (60 ± 8) nm; (b): 3.7 mJ cm^{-2}, (55 ± 5) nm; (c): 7.6 mJ cm^{-2}; (57 ± 13) and (2.5 ± 1.3) nm; (d): 12.1 mJ cm^{-2}, (56 ± 13) and (3.2 ± 1.2) nm, (e): 19.4 mJ cm^{-2}, (54 ± 12) and (3.0 ± 1.3) nm. (Modified from ref. [70]. Reproduced with permission from the American Chemical Society.)

decrease in ΔA occurs and continues at higher power densities. Thus, the threshold energy of size reduction was assigned to 7.3 mJ cm^{-2} [70]. The assignment was consistent with TEM images given in Fig. 11, because the fragmentation started approximately at the same laser power density.

This threshold laser energy cannot be explained by the photothermal mechanism, because the lattice temperature is still far below the bp of gold at this stage (Fig. 10b, $T_L \approx 1300$ K). However, at this laser power density, T_e can exceed the fragmentation threshold of 7300 K for a liquid gold droplet. Thus, it is reasonable to consider that the Coulomb explosion mechanism is applicable.

On the other hand, if we look at the ΔA versus the laser power density profile for a nanosecond-laser excitation, a completely different picture emerges. Fig. 12 is such an example. Since $T_e = T_L$ for the nanosecond-laser excitation, extremely high T_e that exceeds T_e (frag) cannot occur. Instead, the maximum T_L increases steadily with increasing laser power densities, as shown in Fig. 12. Thus, the size-reduction mechanism is described exclusively by the evaporation mechanism that occurs when the particle temperature exceeds the bp.

As stated above, in nanosecond-laser excitation, heat loss to the surrounding medium and the optical effect of bubble formation during the excitation are important. In Fig. 12, the particle temperature curve was constructed considering these two effects. If the heat loss and bubble effect are totally neglected, a considerably different temperature curve can be drawn, especially for the excitation at 532 nm, where the LSPR peak position is located nearby. Fig. 13 shows such an example.

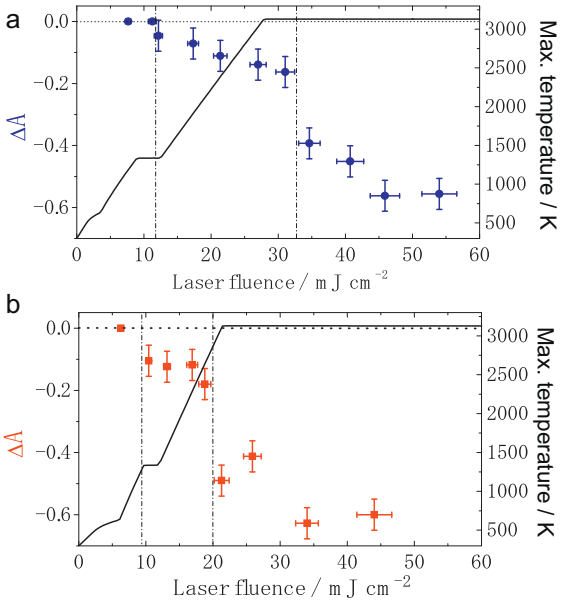

Fig. 12. Laser power density dependent evolution of maximum T_L (solid line) for a 55-nm aqueous gold NP (scale on the right side) together with the experimental plots of ΔA for 36,000 shots versus the laser power density (scale on the left side) on excitation at 532 nm (a) and 266 nm (b). Vertical lines represent the experimental thresholds of melting and evaporation. (Modified from ref. [100]. Reproduced with permission from the American Chemical Society.)

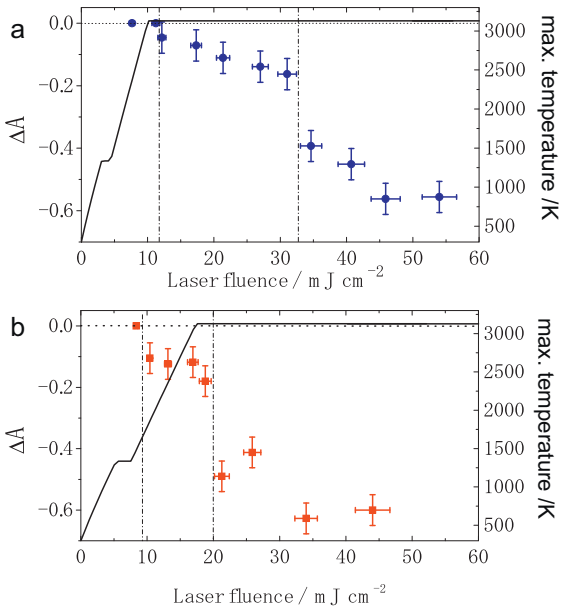

Fig. 13. Temperature curve calculation of maximum T_L (solid line) for a 55-nm aqueous Au NP (scale on the right side) when the heat loss and the optical effect of bubble were neglected, together with the experimental plots of ΔA for 36,000 shots versus the laser power density (scale on the left side) on excitation at 532 nm (a) and 266 nm (b).

Although the experimental size-reduction threshold, i.e., the evaporation threshold for the excitation at 532 nm, is determined as 33 mJ cm^{-2}, the computationally obtained bp is 10 mJ cm^{-2} (Fig. 12a). This large discrepancy is significantly reduced in Fig. 12a in which the computational particle boiling threshold is 28 mJ cm^{-2}. Inspection of Fig. 12b reveals that this discrepancy is small for the excitation at 266 nm. This is because the optical effect of bubble formation is dependent on the excitation wavelength and is not significant at 266 nm (see Fig. 9). It is important to note that previous studies of laser-induced size reduction completely ignored the two effects, which leads to the overestimation of temperature increase [90–99].

The combination of the experimental laser irradiation and computational temperature studies of Au NPs revealed that the nanosecond-laser-induced size reduction can be represented by Scheme 5.

A possible scenario is as follows. During the nanosecond-pulsed-laser heating of Au NPs, thermal energy is transferred to the surrounding water and its temperature, T_m, increases steadily. As the spinodal temperature of 573 K [73] is attained, explosive evaporation of the water occurs and a "hot" high-pressure bubble expands rapidly, which depresses C_{abs} through a refractive-index reduction in the LSPR region. If the laser intensity is sufficiently high to heat up the thermally insulated NPs to the boiling point, surface evaporation, and thus, the size reduction of the original Au NPs results. The generated fragments may form aggregates because of low permittivity within the bubble. Finally, after the nanobubble collapses and the NP cools down to room temperature, the coexistence of size-reduced original NPs and small "snake-like" or "nut-like" structures can be observed in TEM images.

So far only one study has reported the failure of the observation of single-shot femtosecond-laser-induced fragmentation. Warshavski et al. [117] used both 800-nm (50 fs, 150 mJ cm^{-2}, 3×10^{12} W cm^{-2}) and 550-nm (90 fs, 90 mJ cm^{-2}, 1.8×10^{12} W cm^{-2}) laser pulses for the excitation of 16, 23, and 45 nm diameters of Au NPs in aqueous solution. They could not identify any statistically significant decrease in the average particle size by TEM observation. They ascribed the effect of femtosecond pulses as causing no significant particle size reduction. However, the interpretation of an ensemble experiment, in which only a portion of the particles that are exposed to the peak intensity of a laser pulse undergoes complete fragmentation, requires a certain precaution. The particles exposed to the wings of a spatial Gaussian beam may be reshaped rather than fragmented because of insufficient energy absorption.

3.2.4. Time scale of fragmentation

To reveal the time scale of size reduction/fragmentation, transient-absorption spectroscopy was employed by Werner et al. [70]. Previously, femtosecond pump-probe spectroscopy has been applied to elucidate the electron dynamics of plasmonic

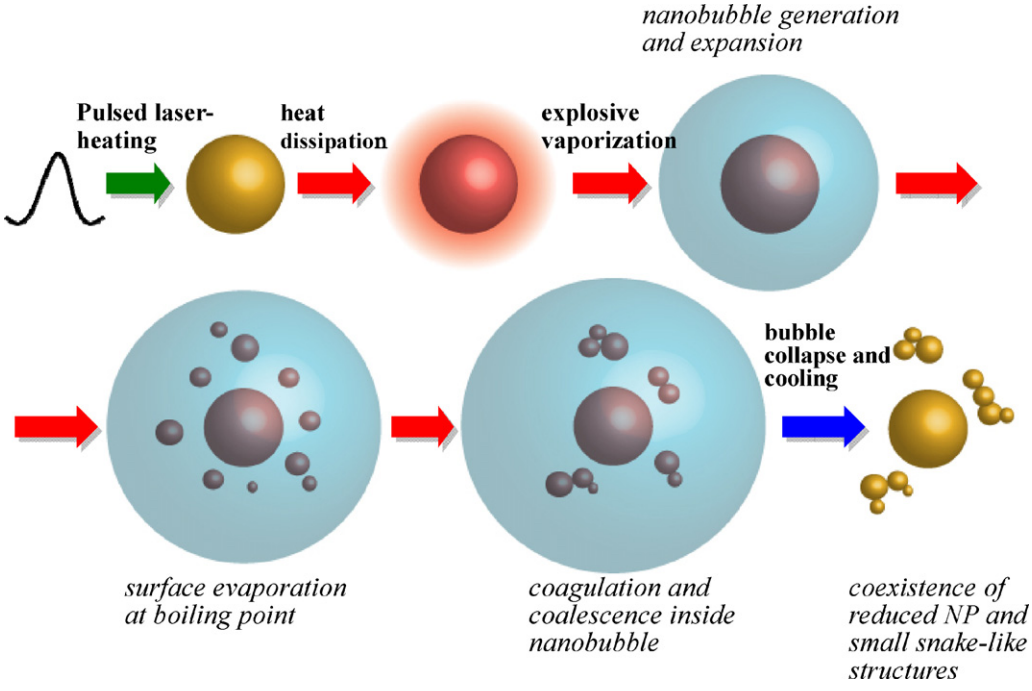

Scheme 5. Schematic illustration of the size reduction of aqueous gold NP colloids by nanosecond-pulsed-laser irradiation.

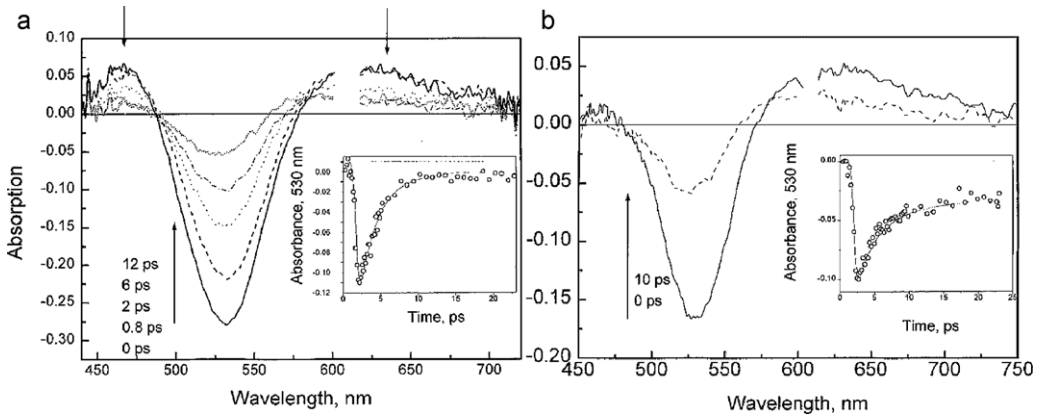

Fig. 14. Transient-absorption spectra of 30-nm Au NPs in water as a function of the time delay between the pump- and probe-(white light) laser beams. The excitation wavelengths are (a) 600 nm (intraband) and (b) 380 nm (interband). The insets show the kinetics of the plasmon band at 530 nm. (Reproduced from ref. [66]. Reproduced with permission from the American Chemical Society.)

NPs [65–67]. Fig. 14 shows an example of transient-absorption spectral changes of Au NPs in aqueous solution. Negative absorption or "bleaching" signals are indicative of ultrafast electron relaxation (cooling) processes (electron–electron relaxation and electron–phonon relaxation processes), mentioned above.

The bleaching signal occurring from initial femtoseconds to several hundred picoseconds may interfere with transient signals associated with laser-induced fragmentation because the size reduction can be observed by the reduction in the LSPR band. However, it is interesting to note that an isosbestic point appears at ≈490 nm in the transient-bleaching signals, as shown in Fig. 14. By exciting 60-nm-diameter Au NPs at 400 nm and probing at 490 nm, the LSPR bleaching signals ascribable to the fragmentation of Au NPs were observed (Fig. 15).

At a laser power density of 3.7 mJ cm^{-2} which is below the fragmentation threshold, only a slightly reduced signal ascribed to a surface melting was observed. At the fragmentation threshold (6.1 mJ cm^{-2}) and above (17.2 mJ cm^{-2}), greater bleaching signals increasing with laser power density were observed and this was ascribed to fragmentation signal. Inspection of Fig. 15 reveals that fragmentation takes place not instantaneously but over 100 ps. This fragmentation scheme was proposed by assuming the Coulomb explosion mechanism as in the following Scheme 6.

On excitation with a laser power density above 6–7 mJ cm^{-2}, high T_e of greater than 7300 K can easily be achieved to induce thermionic electron emission. At the same time, T_L increases to 1337 K, causing a phase transformation from solid to liquid within

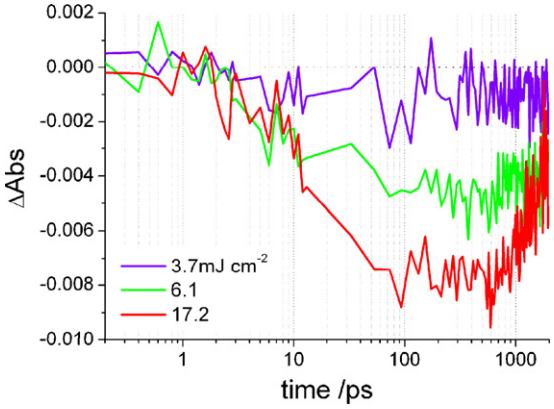

Fig. 15. Femtosecond-transient-bleaching signals at various power densities versus time for 60-nm-diameter Au NPs in aqueous solution measured at (490 ± 5) nm. (Reproduced from ref. [70]. Reproduced with permission from American Chemical Society.)

3–10 ps. This phase transformation greatly decreases the surface tension (surface energy) of the Au NP. When the repulsion energy caused by the critical charge of the liquid Au NP exceeds the Rayleigh instability threshold, the liquid droplet splits into many smaller nanodroplets, that separate into individual clusters in the time course of 100 ps. This is a picture obtained by the transient-absorption study given in Fig. 15.

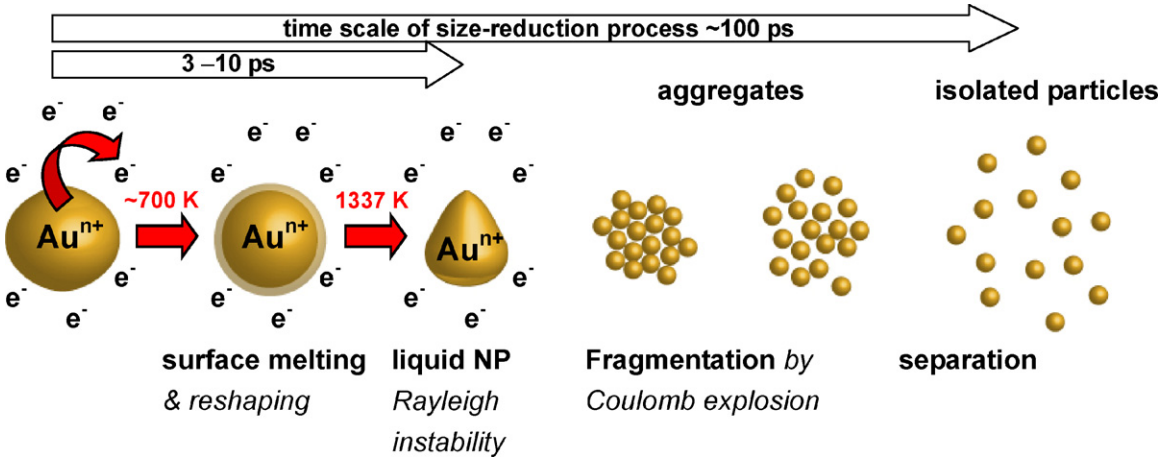

Scheme 6. Schematic illustration representing the femtosecond-laser-induced fragmentation process. (Reproduced from ref. [70]. Reproduced with permission from the American Chemical Society.)

By analyzing the time-resolved Bragg reflection intensity on the irradiation of a 100-fs pulsed-laser ($\lambda = 400$ nm), Plech et al. demonstrated the lattice expansion and melting of 38-nm-diameter Au NPs in water [106]. They reported that the surface ablation of Au NPs occurs at 9–12 mJ cm^{-2} before the complete melting of the particle that occurs at a power density of 15 mJ cm^{-2}. A fragmentation model was proposed that assumes the spallation of Au ions from the surface of the Au NPs within 100 ps of excitation caused by the near-field enhancement of the incident laser light.

3.2.5. Single-particle approach

As we mentioned above, ensemble measurements suffer a drawback in that they only observe an average figure of various events caused by various laser power densities for various particles sizes. Thus a single-particle approach is favored, because it could give an exact and precise picture of a laser-induced event. Along this line, Ito et al. [118,119] conducted the laser-ablation of single 80-nm-diameter Au NPs submerged in water on a glass substrate. The laser manipulation technique [120–122] was used to bring a NP to a desired position on the substrate. The laser irradiation was conducted by irradiating a single-shot or multiple shots of a Nd:YAG laser pulse (355 nm, 6 ns). Atomic force microscopy (AMF) images were recorded before and after the irradiation. The fragmentation threshold of 120 mJ cm^{-2} was determined by the observation of ablation-induced fragments. The threshold value is appreciably higher than that of solution measurements because of substrate effect (see Fig. 12). It was also found that the individual ablation of Au NPs on glass substrates in a solution results in the efficient adhesion of their fragments onto the substrates. This can be used for the formation of patterned NPs on a substrate. For swift and convenient analysis of particles without the aid of AFM, single-particle spectroscopy measurements can be performed to monitor the ablation event by applying dark-field microscopy [59].

3.3. Heat transfer from gold nanoparticles to the surrounding medium

Hu and Hartland [123] investigated the cooling dynamics of Au NPs with various diameters dispersed in water by femtosecond pump-probe spectroscopy. From their experiment, they concluded that the probe signal versus time profile could be conveniently fitted by applying a stretched exponential function, given by

$$F(t) = A \cdot \exp\left[-\left(\frac{t}{\tau}\right)^{\beta}\right] \tag{12}$$

Here τ is the cooling time constant, t is the delay time, and β is the stretching parameter. By fitting the experimental results, they found an almost quadratic dependence of the cooling times on the diameter of the particles, whereas the stretching parameter remained practically constant at 0.7. Fig. 16 shows the Au NP size-dependent cooling time constants.

Hu and Hartland gave an empirical equation for calculating the NP temperature at low temperatures;

$$T(t) = (T_i - T_0) \cdot \exp\left[-\left(\frac{t}{0.159} \cdot R^2\right)^{0.7}\right] + T_0 \tag{13}$$

where T_i is the initial temperature at thermal equilibrium and T_0 is the temperature of the surrounding water.

Subsequently, Plech et al. [89] measured the cooling dynamics by observing the lattice expansion and contraction of Au NPs dispersed in water. They analytically solved a set of two differential heat diffusion equations in the Laplace domain and additionally introduced a thermal heat conductance, h, at the NP–water interface. By fitting their analytical results with the experimentally obtained data, they estimated a heat conductance

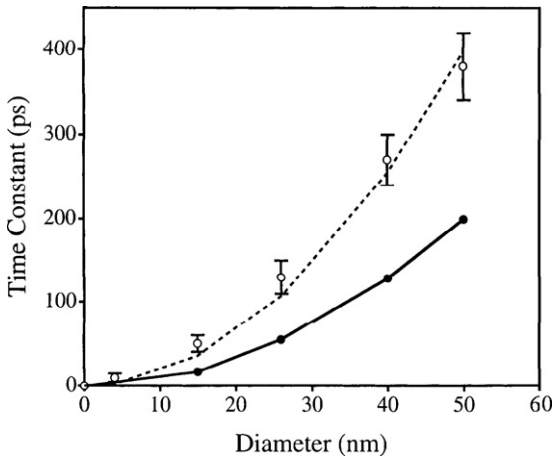

Fig. 16. Characteristic time constant for energy dissipation determined using equation (12) versus diameter: (○) experimental data; (–) calculated temperature versus time profiles. The dashed line shows a fit to the data assuming a parabolic dependence of τ on diameter (i.e., $\tau \propto R^2$). (Reproduced from ref. [123]. Reproduced with permission from the American Chemical Society.)

of (105 ± 15) MW m^{-2} K^{-1}. It was considered that the NP–water interface builds a layer of a few nanometers surrounding the NP surface with an average temperature defined by $T_m(R)$. For a sphere with radius R, the surface area A_P, and the volume V_P, are defined as $A_P = 4\pi R^2$ and $V_P = 4/3\pi R^3$. Thus the heat transfer term at the NP–surface–water boundary, equation (9), reduces to

$$F = \frac{3h}{R(T_L)}\left[T_L - T_m(R)\right]. \tag{14}$$

Equation (14) shows that the heat loss through the NP–water interface is proportional to the temperature gradient between the lattice and water. Furthermore, F is inversely proportional to the NP radius, which consequently leads to an increase in the heat transfer by reducing the NP size. In other words, a strong thermal non-equilibrium exists between T_L and T_m, and smaller NPs have greater heat loss. Depending on the distance from the NP–water interface, the surrounding water medium gives a temperature distribution according to equations (14) and (7c) (or (11b)). Fig. 17 shows an example of the calculated spatial water temperature curves for a 55-nm Au NP excited with different pulse durations, 5 ns and 150 fs, at three different time delays.

Inspection of Fig. 17 reveals that the nanosecond-laser heating of Au NPs leads to a greater heat dissipation to the surrounding water than the femtosecond-laser heating. The lattice and water temperatures at the NP surface–water interface are in *quasi*-equilibrium for the nanosecond case. In contrast, in the femtosecond-laser heating, the effect of heat conductance is clearly visible. At a short delay of 100 ps, a discontinuous decrease is observable in the temperature across the NP–water interface because of the effect of the thermal boundary conductance h: a thermal non-equilibrium of T_L and T_m is established. By increasing the delay time, the difference between T_L and T_m is reduced and vanishes after 600 ps. At this time delay, a thermal equilibrium is attained caused by the cooling of the NP lattice temperature occurring simultaneously with the heating of the surrounding water. Thus, the results show that the finite thermal interface conductance is an important factor for controlling the cooling of metal NPs in condensed media. Molecular dynamic simulations of the heat transfer of Au NPs in different liquids have shown temperature distributions similar to those given in Fig. 17 [124]. The heat conductance of Ag NPs embedded in a glass matrix has been estimated by Juve et al. [125].

An important consequence of the heat transfer to the surrounding liquid of laser-heated metal NPs is the formation of

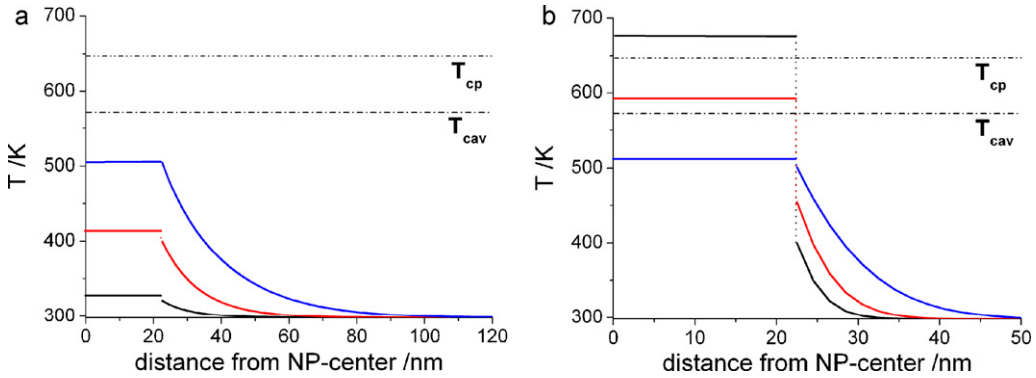

Fig. 17. Calculated temperature profiles of water surrounding a 55-nm-diameter Au NP excited with a laser power density of 2.5 mJ cm^{-2} at (a) 355 nm (pulse duration: 5 ns) and (b) 400 nm (pulse duration: 150 fs) as a function of the radial distance r from the particle center. The time delays are (a) 7.5 ns (black curve), 10 ns (red curve), and 15 ns (blue curve); (b) 100 ps (black curve), 200 ps (red curve), and 600 ps (blue curve). The starting point of the simulation was $-2\tau_P$ from the maximum of the Gaussian time profile. The temperature inside the particle is assumed to be uniform. Temperatures, T_{cp} and T_{cav}, represent the temperatures of water at the critical point (647 K) and the bubble formation threshold (573 K), which considers the spinodal effect of water.

vapor nanobubbles. Plech and co-workers [42,126] experimentally investigated the formation of vapor bubbles by probing the environmental water and its structural change with X-rays after the explosive phase transformation. They estimated that the vapor nanobubble with an initial high pressure expands up to a maximum radius, where the inner pressure is reduced to an equivalent value to the outer water pressure, and then the bubble starts to collapse. The maximum radius greatly depends on the laser power. After the first cycle, the surrounding liquids are heated up again to the critical temperature through heat transfer from the NP surface and another bubble formation occurs. This process is repeated in a sequential manner with a decrease in the maximum bubble radii until the metal NP is cooled down far below the cavitation temperature. An example of measured bubble dynamics by X-ray pump-probe spectroscopy together with the calculated bubble radii and inner pressures by applying the Rayleigh–Plesset equation is given in Fig. 18.

Here the maximum bubble radius is reached after 250 ps, at which time the pressure within the bubble decreased to an equivalent value of the outermost water pressure (1 atm). The first maximum in pressure at 650 ps denotes the collapse of the first bubble. The following calculated modulations in pressure and size are only expected for oscillatory bubble motion.

Subsequently, Plech and co-workers [43] conducted the excitation of Au NPs dispersed in water by a femtosecond-pulsed-laser and observed their lattice contraction during the cooling process. At a certain laser power density and delay time, the NP lattice remained constant without undergoing contraction, where no efficient heat transfer occurred. They assigned this laser power density as the threshold power density of the formation of a nanobubble that thermally insulates the Au NPs. Fig. 19 gives the relative lattice expansion dependent on the laser power density for two Au NP sizes.

Furthermore, they estimated a bubble formation temperature that is slightly dependent on the Au NP size but is approximately equal to the critical point of water (T_{cp} = 647 K).

More recently, Plech's group [127] conducted nanosecond-time-resolved spectroscopy experiments on 60-nm and 80-nm-diameter Au NPs dispersed in water to observe the bubble dynamics. They excited the suspension by single 10-ns pulses at 532 nm or 355 nm to measure the extinction signals with

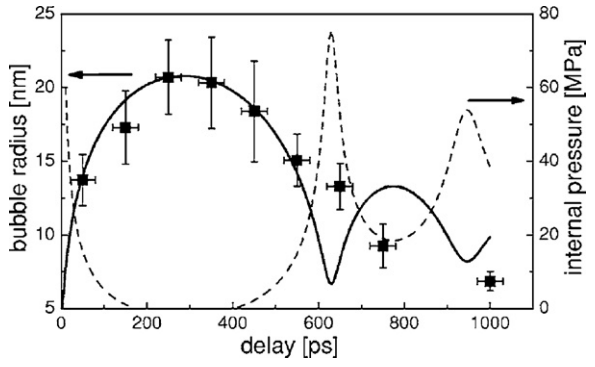

Fig. 18. Bubble radius (solid curve) and pressure (dashed curve) transients of the water vapor inside the bubble as calculated from the Rayleigh–Plesset equation together with the measured radii. (Reprinted with permission from ref. [42]. Copyright 2005, American Institute of Physics.)

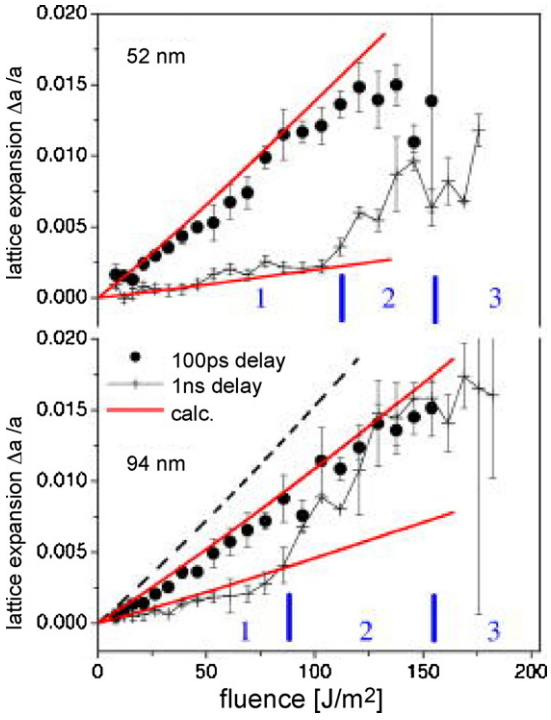

Fig. 19. Lattice expansion of Au NPs of 52- and 94-nm diameters as determined from the peak shift of the (1 1 1) powder reflection at 100 ps (circles) and 1 ns (crosses) delays together with a calculation of the thermal expansion (lines; dashed line without rescaling). Above 155 J m^{-2} (15.5 mJ cm^{-2}), no powder reflection at the 100 ps delay is detectable, indicating particle melting. (Reprinted with permission from ref. [43]. Copyright 2006, American Institute of Physics.)

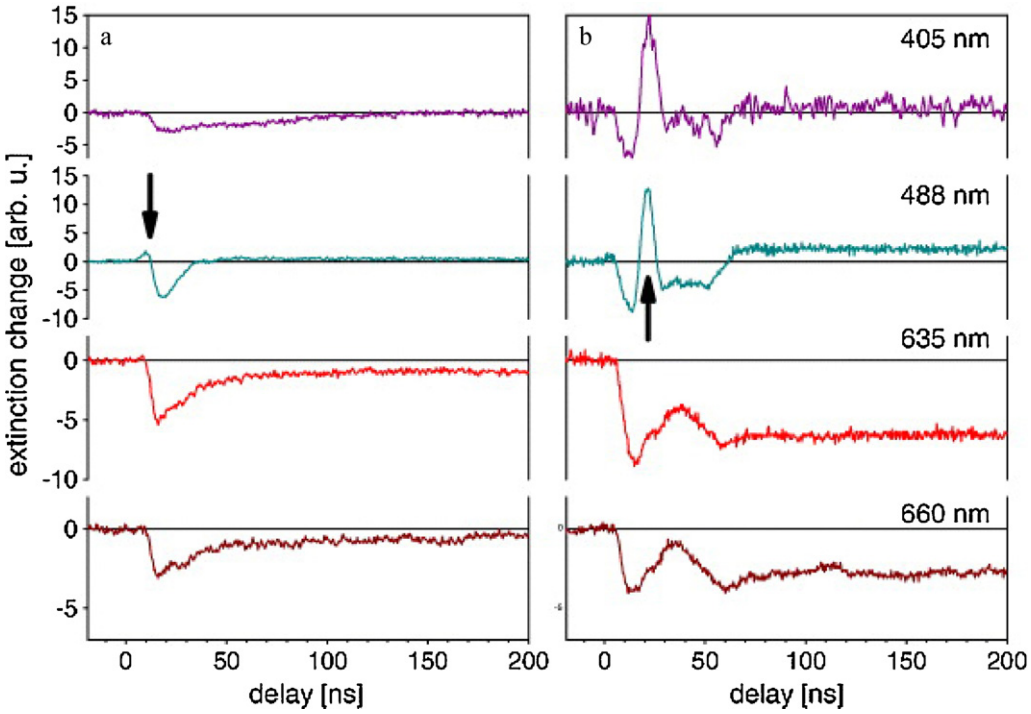

Fig. 20. Transient-extinction change of an 80-nm Au NP suspension by four collinear multicolor laser probe beams excited with a single 10-ns laser pulse at 532 nm at a power density of (A) 300 J m^{-2} (30 mJ cm^{-2}) and (B) 450 J m^{-2} (45 mJ cm^{-2}). (Reproduced from ref. [127]. Reproduced with permission from IOP Publishing.)

nanosecond-time resolution at several wavelengths. They observed an oscillating signal of one period from a negative signal turning to a positive one, which is given in Fig. 20.

Plech's group discussed the detected extinction signals on the bases of the calculated Mie extinction spectra of a Au NP and expanding vapor bubble in water at different temperatures. They concluded that the extinction signal at the threshold laser power density of bubble formation first decreases, because of a reduced extinction of Au NPs caused by a refractive-index change from water to vapor (from 1.33 to 1, see Fig. 9) and a negligibly small extinction signal of small vapor bubbles. At longer time delays, the vapor bubbles grow, leading to an extinction (scattering) signal higher than that of the Au NP extinction at ambient temperature.

The right side of Fig. 21 shows an extinction change $\in(\Phi)/\in(0)|_{t=5ns}$ as a function of the laser power density. A calculation of the extinction as a function of the bubble size is shown on the left. The interpretation assumes that the extinction first decreases on increasing the power density (increasing maximum bubble size) because of the decoupling of the LSPR from the dielectric surrounding. At a larger laser power density, the bubble increases in size and enhances scattering as a positive contribution to the extinction. It should be mentioned that Plech and co-workers applied rather high laser power densities, well above the size-reduction threshold of Au NPs dispersed in water [90,93]. Size reduction and reshaping may lead to a permanent extinction reduction and blue shift of the plasmon band, and thus should be considered in the interpretation of the signal observed here.

Lapotko's group [45,128–130] carried out scattering spectroscopy on a single Au NP placed on a glass substrate surrounded by water. They excited the NP with a single laser pulse with both nanosecond- and subnanosecond-time scale durations. They detected the time-dependent scattering and transmission signals using a CW or pulsed-laser for analyzing light. They found that a much higher laser power density (100 mJ cm^{-2} for a 250-nm-diameter Au) at an excitation laser wavelength of 532 nm is necessary for the threshold of bubble formation than that expected theoretically by employing a simple light-to-heat conversion model. At the threshold of bubble formation, a minimum lifetime of ~9 ns was observed, which was independent of the Au NP diameter. This discontinuity (threshold behavior) could not be detected by replacing the Au NPs with absorbing molecules dissolved in water. In this case, the shortest bubble lifetime measured by a photodetector (transmittance) signal at the vapor bubble generation threshold was ~1.6 ns, and the lifetime increased gradually with increasing laser power densities with a very low threshold. Because of the much higher bubble generation threshold and discontinuity in the minimum lifetime, Lapotko's group considered the phenomenon a new complex nanosystem, i.e., plasmonic nanobubble (PNB). It should be pointed out that they did not consider the possible effects of glass substrate on cooling and bubble nucleation. Fig. 22 shows the laser power density dependent bubble generation probability and lifetime of a 90-nm Au NP.

Lapotko's group discussed the increased threshold for bubble formation on the basis of the curvature effect. According to the Young–Laplace equation, a smaller curvature radius of water yields a higher vapor pressure. This additional pressure has to be overcome before the bubble, which is generated by a laser-heated Au NP, can expand into the surrounding water. In addition, they detected increased scattering or extinction signals by increasing the laser power density. Thus, the lifetime and maximum scattering was directly correlated with the bubble size.

The experimental data of Plech [127] and Lapotko [129] contradict to each other. For instance, one significant difference is the threshold laser power density of bubble formation. Lapotko's group postulated much higher laser power densities necessary for bubble initiation than the theoretically estimated ones. On the other hand, Plech's experimental data agreed well with the thermophysical calculations and the spinodal effect of water. Also, Lapotko did not observe any oscillation-like signals.

Neumann and Brinkmann [44,131,132] conducted experimental investigations on the nucleation dynamics of bubbles in water by the 532-nm pulsed-laser excitation (duration: 12 ns) of

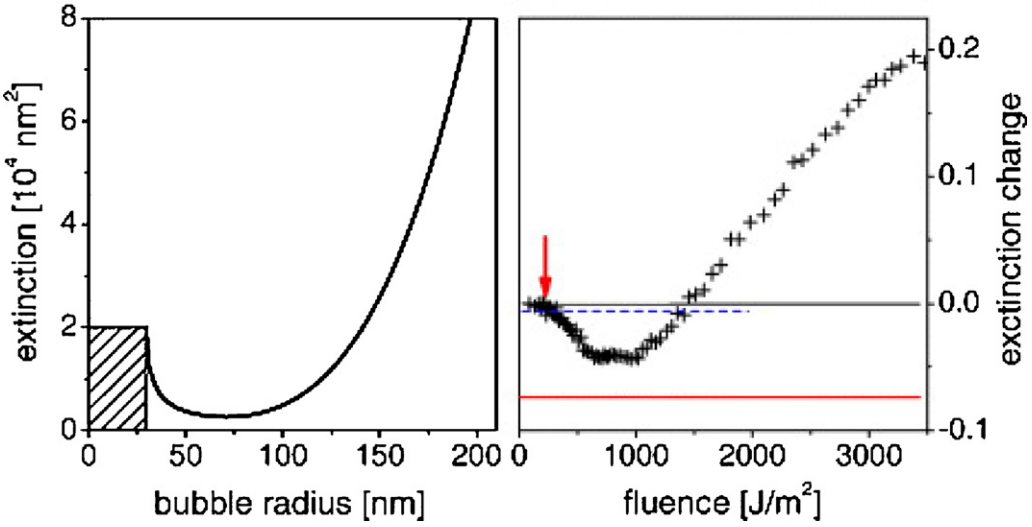

Fig. 21. Left: calculation of the extinction cross section of an Au NP with a radius of 30 nm (60 nm diameter) as a function of a surrounding vapor bubble of variable size. Vertical lines denote the particle–vapor interface. Right: measured extinction change at 532 nm through a 60-nm-diameter Au NP suspension in the flowing capillary at a variable laser power density of 355-nm pulses. (Reproduced from ref. [127]. Reproduced with permission from IOP Publishing.)

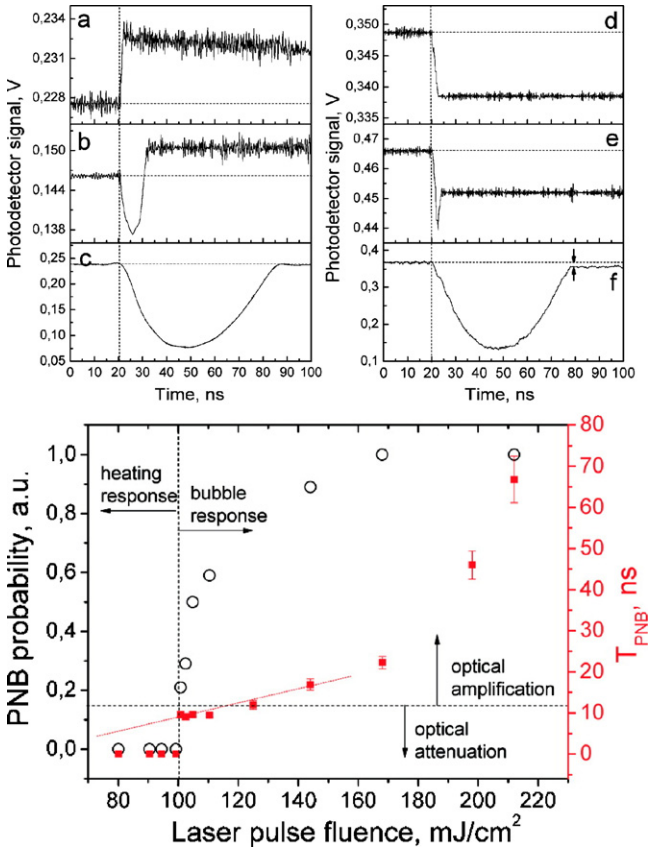

Fig. 22. (A) Time responses for single 80-nm Au NPs (a–c) and a molecular solution of Trypan Blue (d–f) obtained with a single pump-laser pulse (vertical dashed line): (a) subthreshold fluence representing medium heating, (b) near-threshold power density of bubble formation, (c) over-threshold power density showing bubble dynamics, (d) dye absorption, (e) bubble formation power density, (f) bubble dynamics. Two arrows in f show the deviation of the after bubble signal from the baseline caused by residual heating of the surrounding water. (B) Dependence of the PNB lifetime (T_{PNB}, red) and the generation probability (black) around single 90-nm Au spheres on the power density of a single pump-laser pulse (0.5 ns, 532 nm); vertical line separates the types of corresponding time responses (A), and the horizontal line separates the optical scattering effect. (Reproduced from ref. [129]. Reproduced with permission from the American Chemical Society.)

microabsorbers, melanosome. They found a rather low bubble threshold at a temperature of 409 K. They explained the observation by the spinodal effect of superheated water, where the density of water becomes dramatically low (spinodal density) and explosively converts into vapor. In other words, the average distance between the water molecules reaches a critical distance because of the disruption of hydrogen bondings. Furthermore, Neumann's group obtained the bubble radii and expansion velocities from time-resolved microscopy dependent on the laser power density. The velocities ranged from 10 to 85 m s^{-1} for laser power densities that were 1.5–8.5 times greater than the threshold power density. On the other hand, the shock wave velocity, generated by pulse-laser-heated NPs, is approximately the velocity of sound.

The mechanisms of laser-induced bubble formations assisted by nano-/micro-absorbers have not been fully understood. Clear explanations for the experimental results still are needed.

3.4. Laser-induced agglomeration and fusion

Instead of size reduction or fragmentation, the pulsed-laser-induced growth of Au NPs has been observed [133–144]. Kamat and co-workers [133] observed that thionicotinamide-capped Au NPs (particle diameter: 15–20 nm) dispersed in water undergo fusion and fragmentation on laser-pulse excitation (532 nm, ~18 ps, 1.5 mJ pulse^{-1}) for 1 min. The resultant particles had grown in size (~100 nm) but were well separated. After 30 min of continuous laser irradiation, they observed fragmentation of these particles, producing small particles (diameter: 5 nm). They attributed this phenomenon to the melting (fusion) of aggregates to form larger spherical particles because surface-modified Au NPs exist as aggregates. On the other hand, similar laser-induced fusion was not seen in uncapped-Au NPs.

Niidome et al. [136] observe that the irradiation of a pulsed-1064-nm laser light (6–8 ns, 875 mJ cm^{-2}, 10 Hz) to dodecanethiol-passivated Au NPs (3.2 ± 0.92 nm) in cyclohexane resulted in the enormous growth of particles. The size increased up to ~200 nm with spherical shape. In this case, photofragmentation was unlikely, because the smallest particles coexisting were ~10 nm. Removal and/or photodecomposition of the adsorbed dodecanethiol molecules from the particle seems to be indispensable to the fusion of particles. The same group [138] reported

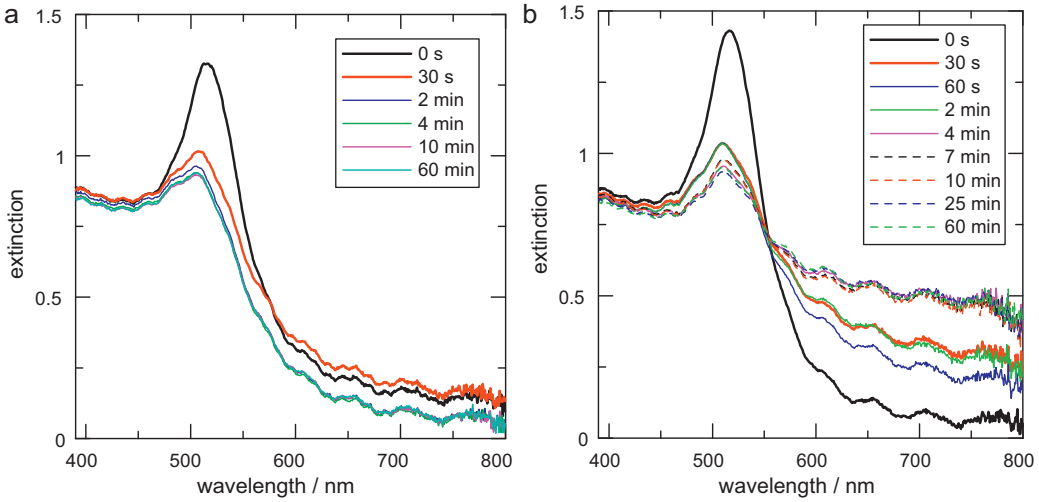

Fig. 23. Laser-induced agglomeration of Au NPs in an aqueous solution by the irradiation of a 532-nm pulsed-laser light (1.1 J cm^{-2} pulse^{-1}, 10 Hz) in a Ar-saturated solution (a), and O_2-saturated solution (b). Au NPs were prepared by the laser-ablation in pure water on irradiation of a 1064-nm pulsed-laser light. (Reproduced from ref. [139]. Reproduced with permission from the American Chemical Society.)

that large and highly spherical Au NPs (diameter: 20–30 nm) can be prepared by a pulsed-laser irradiation (532 nm, 6–8 ns, 10 Hz) of polycation-Au NP (diameter: 10 nm) complexes in an aqueous solution. In this case, the complex of negatively charged Au NPs and cationic poly(diallyldimethylammonium chloride), PDDA was formed by electrostatic interaction. Later, Koshizaki and co-workers exploited this technique for the preparation of submicron-sized spherical particles with a homogeneous size distribution [140–143]. Large spherical particles were also prepared by Pocovi-Martinez et al. [144]. Thiol-passivated Au NPs (3–4 nm diameter) irradiated in chloroform at 266 nm (10 ns, 12 mJ pulse^{-1}) led to a rapid increase (minutes time scale) in the size of NPs, producing large spherical particles (~100 nm).

Werner et al. [139] observed the pulsed-laser-induced agglomeration of Au NPs leading to immediate flocculation in pure water. Notably, they employed uncapped negatively charged Au particles with a broad size distribution (10–100 nm diameter) prepared by the laser-ablation technique [145]. The excitation was provided by a 532-nm nanosecond-laser pulse (laser power density: 1.1 J cm^{-2}). The laser-induced particle growth process was monitored by the extinction growth in the 700–800 nm region at the expense of LSPR band depression. In this case, the size growth occurs simultaneously with size reduction because of the high-intensity laser irradiation. This is the main cause of the observed LSPR band depression. Fig. 23 shows the results.

The growth was seriously affected by the irradiation atmosphere: for instance, the retardation of growth was observed in a Ar-saturated solution while the growth rate was enhanced in a O_2-saturated solution (see the difference between (a) and (b)). The mechanism of agglomeration was ascribed to the combination reaction of cationic fragments generated by the laser-ablation of Au NPs with intact Au NPs with an original negative surface charge to produce large neutral species susceptible to further aggregation. Thus, in water, the role played by the cationic species produced by ablation-induced ionization is very important. In addition, species may be generated, possibly by thermal processes such as melting and vaporization.

Therefore, laser-induced melting, removal of stabilizing ligands, and charge neutralization are mainly ascribed to coalescence (fusion) and agglomeration of particles for pulsed-laser irradiation. Interestingly, it has been known for years that CW laser or lamp irradiations can cause the coagulation of Au and Ag NPs [146–152]. This "photo-induced coagulation" proceeds for over many hours (e.g. 30 h) for uncapped-Au NPs by the irradiation of UV light from a high-pressure mercury lamp or a visible (488 and 514 nm) CW laser beam in organic solvents such as 2-propanol and ethanol [146–150]. Similar light-induced acceleration of aggregation for aqueous Au NPs stabilized by citrate was observed by exciting the LSPR band by a 514-nm CW laser [151]. According to Kimura, photo-enhanced van der Waals attractive force on the excitation of the LSPR band is responsible for the observed phenomena [148,149]. On this point, recent studies that apply an optical-trapping technique deserve comment [153–155]. Yoshikawa et al. demonstrated that the optical trapping by a 1064-nm CW laser can control the assembly of Au NPs (40 nm diameter) reversibly in water [153]. By the action of optical force, the LSPR extinction band of assembled NPs (600–700 nm) was observed to increase with increased laser intensity owing to a conformational change in the Au NP assembly. Zhang and co-workers [155] observed that the optical trapping of micron-sized Au NP aggregates or 40-nm-diameter citrate-capped Au NPs with a CW laser at 532 nm induced irreversible agglomeration. The observed trapping was explained by optical force, in the first place, but they also attributed an additional cause to laser heating.

4. Application of laser-induced response of metallic nanoparticles

4.1. Surface modification and treatment of substrate

Interaction of lasers with plamonic NPs allows nanofabrication on various substrates on which the particles are placed or assembled. Ko and co-workers reported the fabrication of nanometer-sized craters on a polyimide film self-assembled with Au NPs when exposed to a 532-nm nanosecond-laser light through an objective lens (3–5 ns pulse width, 30–300 mJ cm^{-2} power density) [156]. Tsuboi and co-workers observed the nanohole (d < 100 nm) formation on a Au NP–polymer hybrid film deposited on glass substrates and irradiated by a single 532-nm (~8 ns) laser shot [157]. These two studies attributed the origin of nanoholes to a heat-mode fabrication, caused by the heat transfer from the NPs. The heat mode of nanofabrication represents the material modification owing to the damage caused by melting and the explosive evaporation of Au atoms and clusters. The nanoholes were generated through the rapid overheating of strongly absorbing NPs

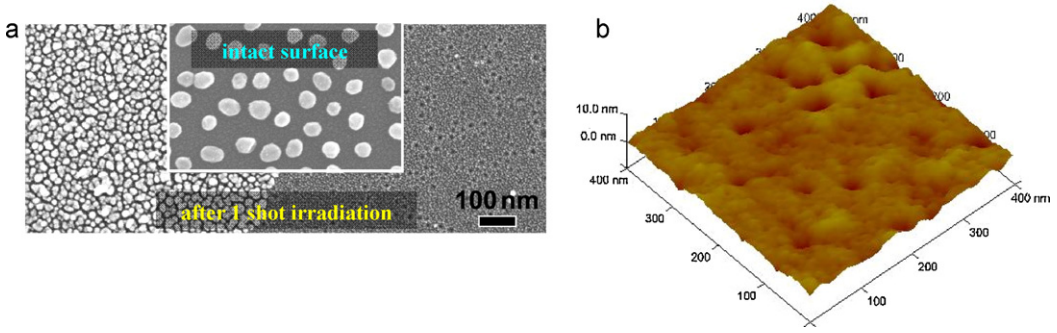

Fig. 24. (a) SEM image of a borosilicate glass surface assembled with 47 ± 8 nm Au NPs with a surface coverage of 30% and exposed to a single-shot of a 532-nm pulsed-laser light (power density: 360 mJ cm^{-2} pulse^{-1}). The left side of the image shows the glass surface fully covered with small NPs resulting from the laser splitting of the original particles. The right side of the image displays a bare surface from which the particles were removed after laser irradiation. Here many dark spots with a slightly bright outer ring are formed on the bare surface. For comparison, the inset depicts the SEM image of the glass surface before the irradiation. (b) AFM topographical images of sample surfaces subjected to a single-shot laser irradiation at a laser power density of 470 mJ cm^{-2}. Dark spots represent pitted areas corresponding to the craters. The average crater depth is 4–6 nm. The AFM images were acquired for the surfaces exposed to the laser irradiation and in the absence of Pt–Pd coating. The fragments of Au particles were removed before the measurement. (Reproduced from ref. [116]. Reproduced with permission from the American Chemical Society.)

during a short laser-pulse duration when the influence of heat diffusion is minimal.

Hashimoto et al. [116,158] observed the formation of nanocraters on a borosilicate glass surface assembled with 40-nm-diameter Au NPs when irradiated with a single-shot nanosecond-pulsed-laser with a wavelength of 532 nm (Fig. 24). Laser power densities of two orders of magnitude smaller than those of causing the breakdown of the glass were applied for the fabrication of the craters.

The average diameter of the craters was ~20 nm with a depth of less than 10 nm for the single-shot experiment: however, after repeated irradiations, the size of the craters expanded to a 100 nm scale [158]. The crater formation was simultaneous with the laser-induced splitting of Au nanoparticles to generate smaller particles of 15 nm diameter. The number density of the craters increased sharply, depending on the laser power density. The onset of the increase occurred at ~160–170 mJ cm^{-2} pulse^{-1}, and reached a value of two times the number density of original Au particles (150 ± 10 particles·μm^{-2}) with a weak tendency to level off at high power densities (Fig. 25a). The onset of the crater formation coincides with the splitting of Au NPs because of increase in the temperature above the boiling point (~3100 K) of gold resulting from the absorption of the laser energy. Thus, the explosive evaporation of gold nanoparticles is postulated to play a crucial role for the modification observed here. This assumption gained a support from the estimation of laser power density dependent thermoacoustic pressures due to the sudden evaporation of gold (Fig. 25b).

This finding may represent a new application of the laser-ablation/fragmentation of nanoparticles to material processing based on the photothermal process. Very recently, Tsuboi and co-workers have demonstrated that this laser-Au NP technique is applicable to the formation of pores on the shell wall of spherical hollow silica microparticles embedded with Au NPs [159]. They prepared pores of tunable sizes from 17 to 56 nm by varying the size of original Au NPs from 6 to 39 nm.

In the meantime, Obara and co-workers observed the formation of nanoholes on the surface of a silicon substrate placed with 200-nm-diameter Au spheres by irradiating a single femtosecond-laser pulse (800 nm) with an intensity of less than the ablation threshold of silicon [160–162]. Leiderer and coworkers observed the ablation pattern for regular arrays of gold triangles with a side length of 450 nm and a thickness of 25 nm when these structures were illuminated with a 150-fs laser pulse (800 nm, 10 mJ pulse^{-1}) [163,164]. Holes as small as 5 nm were fabricated at two corners of each triangle on a silicon substrate. Heltzel et al. observed

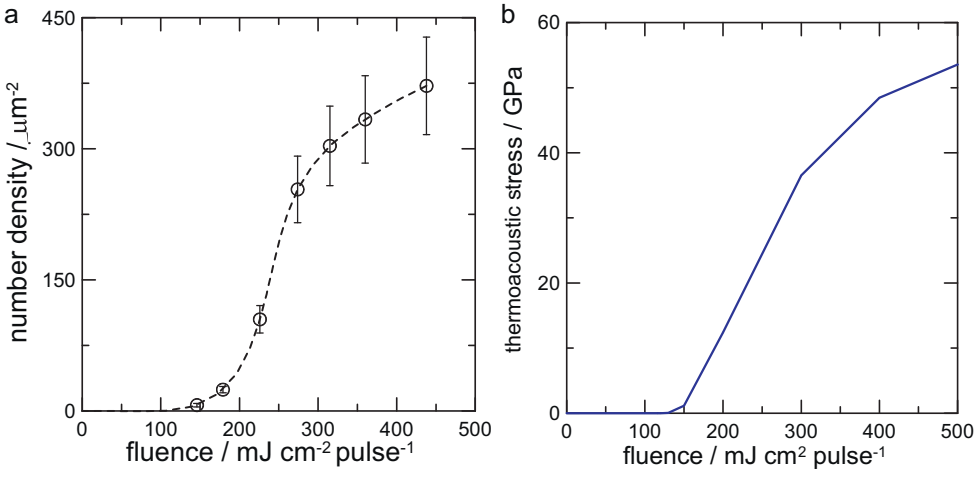

Fig. 25. (a) Number density of craters as a function of the laser power density for single-shot laser irradiation. The number density of original Au NPs was (150 ± 10) particles μm^{-2}. (b) Thermoacoustic pressure estimated by the vapor pressure of gold given by $p_0 = \left((2\pi m)^{3/2}/(k_B T)^{1/2}\right) \nu_0^3 \cdot \exp\left(-L_0/k_B T\right)$ as a function of the laser power density of 45-nm-diameter Au NPs placed on a glass substrate (effective refractive index: 1.12). In the equation; m, ν_0; L_0; and k_B represent the atomic mass of gold; lattice vibration frequency; sublimation energy; and Boltzmann constant, respectively. (Reproduced from ref. [116]. Reproduced with permission from the American Chemical Society.)

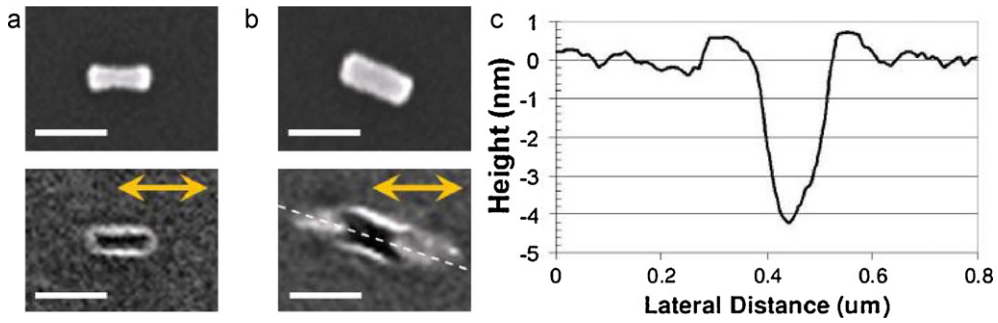

Fig. 26. Nanoscale-ablation site and depth profile: SEM images of the nanorods before and after laser irradiation at a local effective power density of (a) 54 mJ cm^{-2}, right at the ablation threshold, and (b) 218 mJ cm^{-2}. The scale bars correspond to 75 nm, and the yellow arrows indicate the incident polarization. (c) The depth profile of the ablation site shown in (b), along the long axis shown with the dotted line as obtained using AFM. Note the different scales for the horizontal and vertical axes in (c). (Reproduced from ref. [76]. Reproduced with permission from the Optical Society of America.)

nanoholes with a diameter slightly smaller or roughly the same as that of the spheres on a silicon surface with 250- and 40-nm Au nanospheres exposed to a single pulse of a 532-nm nanosecond laser [165]. These observations were attributed to the plasmonic enhancement of the incident electric field at the boundary of the NP and the substrate. This deduction was supported by the observation that the nanohole profiles resembled the laser intensity distribution on the substrate surface in the power density region lower than the ablation threshold power density of the bulk silicon. The assumption of the plasmonic enhancement was also supported by the fact that the holes produced by a linearly polarized wave of laser radiation exhibited an elongated entrance shape in the direction of polarization. Thus, besides the heat mode of enhanced material fabrication, a photon-mode process is postulated to occur, in which the electric field enhancement due to the excitation of the LSPR band of NPs can cause a multiphoton absorption, leading to the ablation and modification of the material surface [160–167].

Despite demonstrations by several groups, the direct cause of plasmon-assisted near-field ablation is still not understood very well. Ben-Yaker's group conducted further research to gain a better understanding of the phenomena [76]. They observed nanoscale-laser modification and ablation of a silicon (1 0 0) surface at local power densities significantly lower than the direct femtosecond-laser-ablation region of silicon, i.e., 420 mJ cm^{-2}. Fig. 26 shows SEM images of ablation sites and a depth profile, as observed by an AFM (atomic force microscopy).

Ben-Yaker's group found that the nanorod ablation sites were a photo imprint of the nanorod, very similar in size to the nanorod. The ablation sites did not consist of two separated craters, which is expected from a calculated $|E|^2$ enhancement pattern. On the basis of this observation, they concluded that the Poynting vector enhancement more accurately predicts plasmonic-laser-ablation than the $|E|^2$ enhancement pattern [76]. However, based on the observation of a double-crater shaped hole, Meunier's group strongly opposed this view [168]. This dispute should be resolved by further experimental and theoretical studies.

Ueno et al. [28,29,169–171] have demonstrated a new technique of nanogap-assisted surface plasmon nanolithography. They prepared arrays consisting of pairs of closely spaced gold nanoblocks on dielectric substrates including glass. They observed the two-photon absorption (TPA)-assisted photopolymerization of a negative-type photoresist, SU-8 in the intense near-field supposed to exist in the nanogap between the blocks generated by the irradiation of a halogen lamp (wavelength range: 600–1000 nm, 0.2 W cm^{-2}), with a CW laser (785 nm) or femtosecond laser (800 nm) [28]. The photoresisit, SU-8 is known to photopolymerize by exposure to ultraviolet light at wavelengths shorter than 360–400 nm, and thus, the simultaneous absorption of two photons is prerequisite to initiate polymerization. Fig. 27 shows the SEM images of pairs of Au nanoblocks, (a) with regions of polymerized SU-8 ((b) and (c)) resulting from exposure to a femtosecond Ti:sapphaire laser (120 fs, 800 nm, 80 MHz).

When the laser beam was polarized linearly along the axis of the pairs (Fig. 27b), longitudinal plasmon modes localized in the nanogaps induced significant local polymerization after a short exposure. When the laser beam was polarized perpendicular to the axis of the pairs, transverse plasmon modes were excited

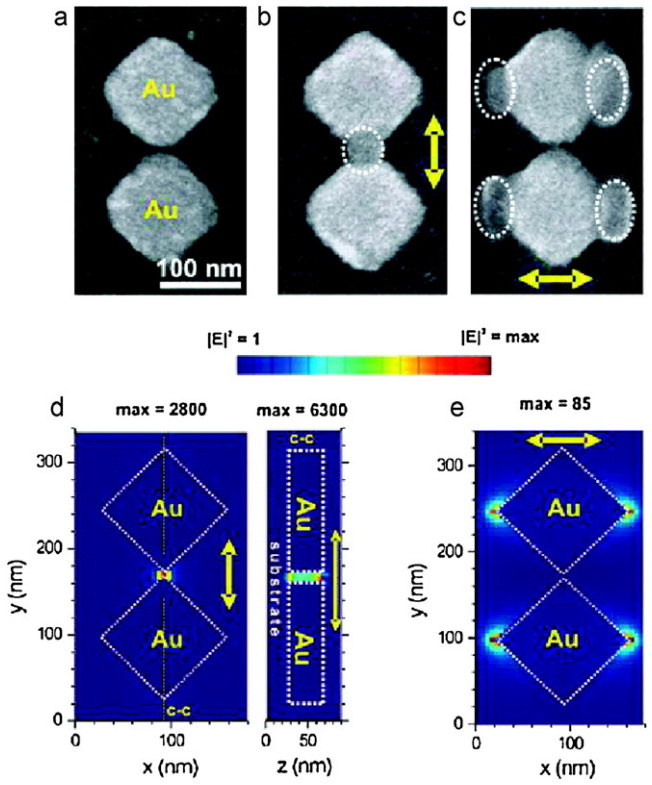

Fig. 27. (a) SEM image of a pair of gold nanoblocks measuring 100 × 100 × 40 nm^3 and separated by a 5.6-nm wide nanogap before irradiation by an attenuated femtosecond-laser beam. (b) SEM image of other nanoblock pairs after 0.01 s exposure to the laser beam polarized linearly along the long axis of the pair. (c) SEM image of another pair after 100 s exposure to the laser beam polarized in the perpendicular direction (d and e). Theoretically calculated near-field patterns at selected planes for the excitation conditions of the samples shown in (b) and (c), respectively. In (d), the field pattern is shown on the *x*–*y* plane bisecting the nanoblocks at half of their height (i.e., 20 nm above the substrate), and in (e), the field is calculated on the plane coincident with the line c–c shown in (d). The field intensity is normalized to that of the incident wave, and therefore represents the intensity-enhancement factor. (Reproduced from [28]. Reproduced with permission from the American Chemical Society.)

and induced photopolymerization in the corresponding regions (Fig. 27c). The calculated field-intensity patterns shown in Fig. 27d and e correspond closely with the experimental photopolymerization pattern. Furthermore, for Au nanoblock structures with nanogaps narrower than 10 nm, photopolymerization rates were increased by orders of magnitude [169]. The same group [170,171] also used the nanoblock structures for photomasks for contact exposure of a positive photoresist on glass substrates. As expected, periodic patterns of pits were formed at the nanogaps in the developed photoresist surface after exposure to a femtosecond-laser beam. It was shown that the ordered clusters of nanoparticles separated by nanogaps can provide a stable and versatile platform for further development of optical subwavelength nanolithography.

LSPR-assisted laser nanofabrication and nanogap-assisted surface plasmon nanolithography are promising techniques to beat the diffraction-limited resolution (200–300 nm).

4.2. Laser-induced deposition and treatment

Niidome and co-workers [137,138,172] reported that Au NPs can be deposited on a glass surface by using nanosecond-pulsed 532-nm laser irradiation (83 mJ cm^{-2} pulse^{-1}) of dodecanethiol-passivated Au NPs (3.2 ± 0.95 nm) in cyclohexane. When laser irradiation was carried out using a photomask, reddish rectangular patterns based on the deposited Au NPs can be clearly observed by the naked eye. The deposition of Au NPs occurs only at the laser-irradiated region of the substrate. The observation is reminiscent of the study conducted by Ito et al. [118,119] for a single Au NP (see Section 3.2.5).

A dense monolayer of isolated Ag- and Au NPs 40–60 nm in average diameter were prepared on mica by converting sputter-deposited Ag- and Au-island films by nanosecond-laser irradiation at 532 nm (~50 mJ cm^{-2}) [173]. Fig. 28 shows such an example. Besides the shape change, particle growth was observed. The resultant film gave strong LSPR bands without any serious broadening. A relatively narrow range of laser power density was employed for the preparation. This power density range corresponds to the particle temperatures between the melting and boiling points of Au NPs, suggesting that particle melting triggers the transformation observed.

In a higher laser power density regime greater or above 100 mJ cm^{-2}, a complicated mode of film conversion resulting in the strong deformation (flattening) of the LSPR band became dominant before the ablation mode finally set in. The fabrication of sphere-like Au NPs of similar shapes and alignments on sapphire, GaN, SiO_2, and silicon substrates by irradiation of a few UV laser pulses on a Au thin film was reported by other groups [174–176].

The nanostructural change to a periodically arranged line pattern with a modified particle size and shape distribution occurred when thin films containing Au NPs were irradiated with femtosecond linearly polarized laser pulses (150 fs) [177]. Fig. 29 shows an example.

A linear dependence between the period Λ of the line structures and the laser wavelength λ (800, 528, 400, and 266 nm) was observed. For the particle size and shape changes, the atomic diffusion process (Ostwald ripening, coalescence/reshaping) was assumed. Photothermal melting/evaporation could be the driving force of the event. The periodic structure is reminiscent of the "ripple" or LIPSS (laser-induced periodic surface structure) that has been formed on nearly every kind of solid material (metals, semiconductors, glasses, and polymers) [178–180]. It was assumed that the constructive interference between incident waves and surface waves generated by the scattering of the incident wave caused the observed surface structural change [178]. The periodically arranged line pattern could be an example of the self organization of Au NPs resulting from the laser-induced photothermal effect. Here it is pertinent to note that Obara and co-workers [181] presented computational and experimental results on plasmonic and Mie scattering control of far-field interference for regular ripple formation on semiconductor and metal. They observed the interference ripple pattern on the silicon substrate, which originates from the plasmonic far field by gold nanospheres irradiated by femtosecond-laser pulses. Their result suggests that in addition to plasmonic scattering, the Mie scattering far field also play a role for the origin of surface ripple formation.

Nanosecond- and femtosecond-laser-induced detachment was observed for Au nanostructures prepared on a silicon or quartz substrate by nanosphere lithography [182–184]. Laser-induced melting was considered to be responsible for the nanosecond excitation because of the contraction of the liquid toward a sphere [182]. The detachment was observed for femtosecond-laser excitation in both air and liquid. The ejection mechanism in air was considered to involve the ablation of surface atoms from a gold particle, which generated intense pressure at the particle–substrate interface [183]. In contrast, in a liquid environment, a mechanism was postulated that involves energy transfer from a photoexcited nanoprism to the solvent within cavities and defects at the particle–substrate interface [184]. In this instance, the hot-solvent molecules result in an intense pressure at the particle–substrate interface, resulting in particle ejection.

4.3. Miscellaneous applications

The optical-limiting effect that strongly decreases the transmission of light at higher laser intensities was observed for Ag nanoclusters and Au NPs dispersed in solution [185–190]. The optical-limiting behavior is applicable to devices that protect human eyes and solid-state sensors from intense optical beams. Fig. 30 shows an example of a dendrimer nanocomposite of Ag clusters, $\{Ag(0)\}_E$.

The nonlinear transmission was observed at 532 nm, within the LSPR resonance spectral range. The threshold power density for optical limiting was 2.0 J cm^{-2}. The mechanism of optical limiting was ascribed to the formation of nanobubbles. The optical-limiting performance of $\{Ag(0)\}_E$ is compared well with the results obtained with carbon nanotubes. More recent nanosecond studies expressed rather controversial opinions [188–190]. While Polavarapu [188] concluded that nonlinear scattering plays an important role in the optical-limiting behavior of oleylamine-capped Au NPs, Sun's group [189,190] postulated the dominant contribution of free-carrier absorption for Au NP aggregates.

Because of chemical and thermal stabilities with less cytotoxicity, plasmonic NPs have been popular in biomedical applications. In particular, the sharp molecular-scale confinement of high-temperature regions is very beneficial as a nanoheater. For example, Takeda et al. [191,192] demonstrated that the degradation of proteins and nucleic acids can result from 532-nm nanosecond-laser excitation (10 ns, 94 mJ cm^{-2} pulse^{-1}) of Au NPs an aqueous solution. For instance, they mixed Au NPs (diameter: ~20 nm) with two kinds of protein molecules: bovine serum albumin (BSA) and lysozyme. Proteins were selectively adsorbed on Au NPs by adjusting the pH of the solution. They observed selective degradation because the Au NP creates a high-temperature region in its close vicinity by the laser irradiation. At the laser power density they employed, the fragmentation/size reduction of NPs is also likely. On the other hand, they assumed that the formation of the laser-induced bubble is unlikely. Before these studies, a similar study had been conducted by Huttmann et al. [193]. Under irradiation with nano- and picosecond-laser pulses, the enzymes alkaline phosphatase and chymotrypsin bound to the surface of 15-nm-diameter Au NPs were inactivated. In this case, clear evidence of

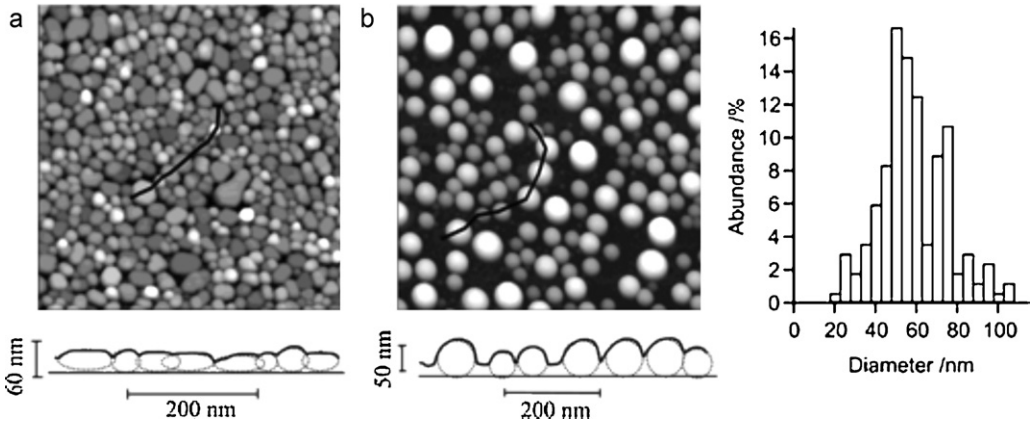

Fig. 28. (a) AFM image (dimensions: $1000 \times 1000\ nm^2$) of an as-deposited Au-island film consisting of flat-shaped particles as simulated below the image. (b) $1000 \times 1000\ nm^2$ AFM image taken after laser irradiation (single-shot at $\sim 50\ mJ\ cm^{-2}$), clearly providing evidence for conversion to good spherical nanoparticles, with a typical height profile and size distribution shown below the image and on the right, respectively. (Reproduced from [173]. Reproduced with permission from the American Chemical Society.)

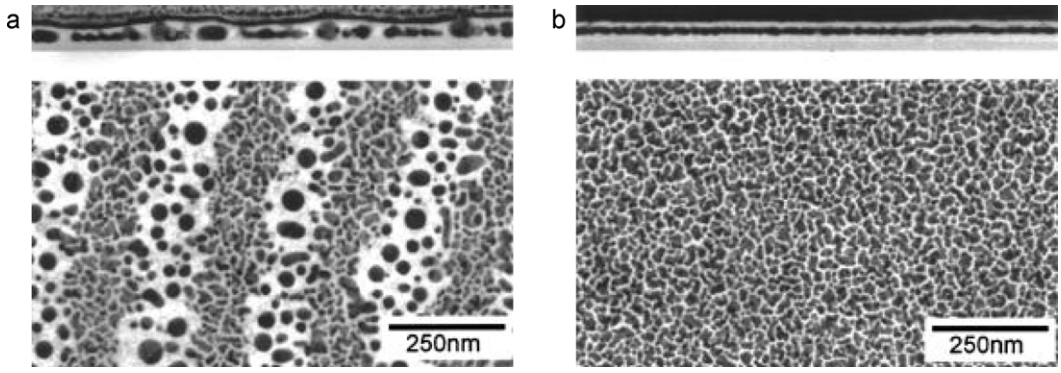

Fig. 29. (a) TEM images (upper: cross-sectional view, lower: overhead view) of a polymer film containing gold nanoparticles after laser irradiation ($\lambda = 400$ nm) and (b) TEM images of a nonirradiated polymer film containing gold nanoparticles. (Reprinted with permission from ref. [177]. Copyright 2005, American Institute of Physics.)

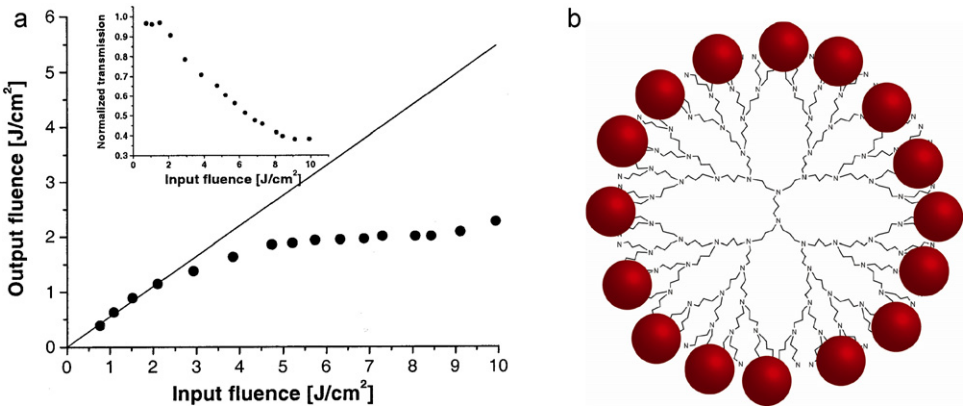

Fig. 30. (a) The optical-limiting behavior of the $\{Ag(0)\}_E$ nanocomposite at 532 nm for a 10-Hz pulse-repetition rate observed by irradiating nanosecond-laser pulses. The solid line illustrates the case of a constant transmission of ~60% (the transmission value at low power density). The inset shows the corresponding transmission variation with the input power density. (b) A schematic representation of dendrimer nanocomposite of Ag clusters, $\{Ag(0)\}_E$ architecture. (Modified from ref. [185]. Reproduced with permission from the American Chemical Society.)

the fragmentation was obtained by TEM measurement. However, they reserved the judgment with regard to bubble formation as a damage mechanism. The involvement of bubble generation with protein deactivation is still not clear.

Another example of a biomedical approach is the application of nanobubbles to theranostics (diagnostics and therapeutics) [194,195]. A distinct goal of theranostics is to selectively target specific (diseased) tissues or cells to increase diagnostic and therapeutic accuracy. In an example shown in Fig. 31 [194], a single-shot laser-pulse excitation of transient and localized vapor bubbles (defined as PNB [45]) caused damage to living cells (lung carcinoma cells A549) using Au NPs.

For each cell, bright field and side scattering optical images were registered before and after the pump pulse. In Fig. 31, picture (a) shows the bright-field image before irradiation and (c) shows it after the irradiation. Also, (b) is the scattering image of PNBs generated inside the cell. The detection of cell damage was based on the observation of blebbing bodies in the bright-field image of the cell after the pulse (c). The study revealed conditions necessary for the precise excitation and

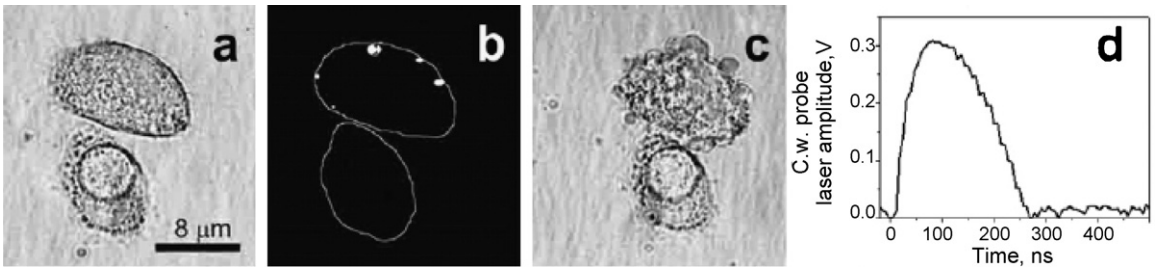

Fig. 31. In vivo generation and detection of plasmonic nanobubble (PNB) in Au NP-treated A 549 cells: (a) bright-field microscopy image of two cells prior to their exposure to a single pump-laser pulse (532 nm, 0.5 ns, 200 mJ cm^{-2}); (b) time-resolved scattering image of the intracellular PNBs obtained with the 10-ns delayed (relative to the pump-laser pulse) pulsed-probe laser (690 nm, 0.5 ns), where the lines show the contours of the cells as in (a); (c) bright-field microscopy image of two cells obtained 120 s after their exposure to a single pump-laser pulse and the generation of PNBs; (d) time response obtained during the exposure to a single pump-laser showing bubble expansion and collapse. (Reproduced from ref. [194]. Reproduced with permission from IOP Publishing.)

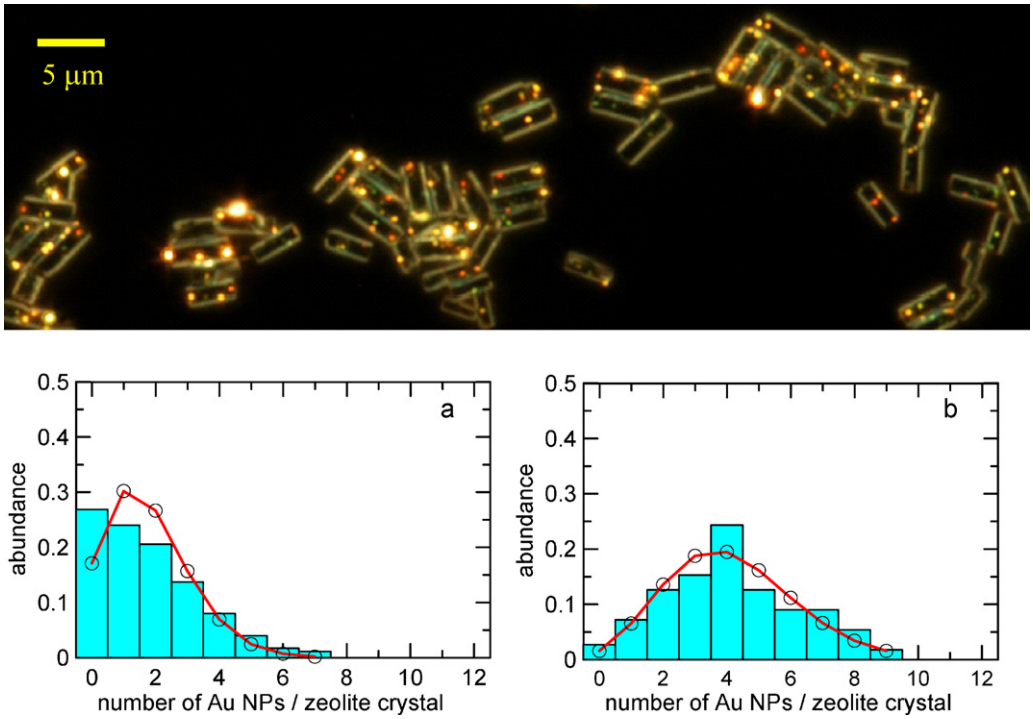

Fig. 32. Upper panel: dark-field light-scattering images of Au NP-doped zeolite L crystals. Lower panel: plots of the number of Au NPs per zeolite crystal (occupancy) versus abundance for different quantities of Au NPs in zeolite crystals. Bar charts show experimental results for approximately 200 zeolite crystals; line plots show calculated curves based on a Poisson distribution for various experimental average occupancies: (a) 1.8; (b) 4.2. (Reproduced from Ref. [197]. Reproduced with permission from the American Chemical Society.)

detection of plasmonic effects in vivo around Au NPs with nanoscale sensitivity.

Finally, we show an example of composite-material fabrication based on laser-ablation generation of Au NPs in liquids [101–105]. Chemically prepared Au NPs are unstable in aqueous solutions containing high concentrations of salts or at extreme pHs. In zeolite synthesis, Au NPs are required to withstand extreme high salts and high pHs. Laser-ablation-based Au NPs were found to be very stable in zeolite synthesis gel containing highly concentrated alkali presumably because of surface negative charge [145]. The upper panel of Fig. 32 shows dark-field light-scattering images of Au NP-doped zeolite L crystals [196,197]. Various colors (yellow, green, orange, and red) of bright spots in the crystals represent Au NPs with various sizes. For instance, green, yellow, and red represent 30–50 nm, 60–80 nm, and greater than 100-nm-diameter NPs, respectively. The measurement of single-particle scattering spectra of each spot is feasible; the particle diameter can be estimated by the simulation of the spectra with the Mie calculation. The lower panel of Fig. 32 represents the histograms of the number densities of Au NPs per zeolite crystal. The number density can be altered by changing the concentration of Au NPs in the synthesis gel. Notably, the histograms were approximated by the Poisson distribution. Beside this example, the laser-ablation-based preparation of NPs in solution may find many other applications.

5. Summary and future outlook

This review demonstrates the immense potential of Au NPs when used with lasers, providing multiple varieties of research opportunities, many of which are ongoing. The beneficial outcome of the researches can influence various fields of science and technology: physics, chemistry, biomedicine, and materials science. The reader may find the key word “LSPR” repeated many times in this review. LSPR is primarily characterized not only by its distinct color but also by its highly efficient light-gathering ability and swift/efficient light-to-heat conversion capability. Regarding the mechanistic side, both ultrafast femtosecond and conventional nanosecond lasers contributed enormously to reveal the dynamics

and processes initiated by the excitation of Au NPs. Although these dynamics have been largely unraveled for the ensemble of particles because of the effort of many researchers, investigations to develop better understanding of the single-particle level with better time resolution is still needed. Additionally, bubble dynamics is currently the most intriguing subject and needs significant effort to reveal the complete picture. From the perspective of materials, we observed the powerful nature of pulsed lasers in combination with Au NPs. Both constructive and destructive effects were demonstrated. The former can be the photothermal fabrication of homogeneous spherical particles, NP monolayers on substrates, periodic structures, and composite materials. Here heat management is crucial to successful fabrication. The latter might be the explosive evaporation, spallation, and fragmentation of Au NPs together with bubble formation. However, in addition to already established destruction of malignant cells, this can be exploited for the fabrication of nanoholes. Photothermal bubbles have potential use in material fabrication and diagnostic/therapeutic applications. Because of remarkably high-resolution properties, plasmon-assisted nanofabrication and nanolithography continue to be a subject of intense research. We will undoubtedly observe further activities and many beneficial results in the laser-plasmonic NP research field for many years to come.

Acknowledgements

KAKENHI (no. 23310065 and no. 22655043) to S. H. from the Japan Society for the Promotion of Science (JSPS) is gratefully acknowledged. JSPS fellowship to D. W. is gratefully acknowledged. Professor Hiroshi Masuhara is acknowledged for his continuous support and encouragement.

References

[1] U. Kreibig, M. Vollmer, Optical Properties of Metal Clusters, Springer, Berlin, 1995.
[2] P. Mulvaney, Langmuir 12 (1996) 788–800.
[3] C.F. Bohren, D.R. Huffman, Absorption and Scattering of Light by Small Particles, Wiley, New York, 1983.
[4] S. Link, M.A. El-Sayed, J. Phys. Chem. B 103 (1999) 8410–8426.
[5] S. Link, M.A. El-Sayed, Int. Rev. Phys. Chem. 19 (2000) 409–453.
[6] G.V. Hartland, Chem. Rev. 111 (2011) 3858–3887.
[7] C. Burda, X. Chen, R. Narayanan, M.A. El-Sayed, Chem. Rev. 105 (2005) 1025–1102.
[8] S.A. Maier, M.L. Brongersma, P.G. Kik, S. Meltzer, A.A.G. Requicha, Adv. Mater. 13 (2001) 1501–1505.
[9] W.L. Barnes, A. Dereux, T.W. Ebbesen, Nature 424 (2003) 824–830.
[10] K. Sokolov, M. Follen, J. Aaron, I. Pavlova, A. Malpica, R. Lotan, R. Richards-Kortum, Cancer Res. 63 (2003) 1999–2004.
[11] C.J. Murphy, A.M. Gole, J.W. Stone, P.N. Sisco, A.M. Alkilany, E.C. Goldsmith, S.C. Baxter, Acc. Chem. Res. 41 (2008) 1721–1730.
[12] S. Lal, S.E. Clare, N.J. Halas, Acc. Chem. Res. 41 (2008) 1842.
[13] X. Huang, P.K. Jain, I.H. El-Sayed, M.A. El-Sayed, Laser Med. Sci. 23 (2008) 217–228.
[14] J. Kneipp, H. Kneipp, K. Kneipp, Chem. Soc. Rev. 37 (2008) 1052–1160.
[15] L. Brus, Acc. Chem. Res. 41 (2008) 1742–1749.
[16] K.A. Willets, R.P. Van Duyne, Annu. Rev. Phys. Chem. 58 (2007) 267–297.
[17] J.N. Anker, W.P. Hall, O. Lyandres, N.C. Shah, J. Zhao, R.P. Van Duyne, Nat. Mater. 7 (2008) 442–453.
[18] K.M. Mayer, J.H. Hafner, Chem. Rev. 111 (2011) 3828–3857.
[19] M. Graetzel, J. Photochem. Photobiol. C Rev. 4 (2003) 145–153.
[20] A.C. Mayer, S.R. Scully, B.E. Hardin, M.W. Rowell, M.D. McCehee, Mater. Today 10 (2007) 28–33.
[21] P.V. Kamat, J. Phys. Chem. C 112 (2008) 18737–18753.
[22] H.A. Atwater, A. Polman, Nat. Mater. 9 (2010) 205–213.
[23] S. Gao, K. Uno, H. Misawa, Acc. Chem. Res. 44 (2011) 251–260.
[24] P. Bharadwaj, B. Deutsch, L. Novotny, Adv. Opt. Photon. 1 (2009) 438–483.
[25] V. Giannini, A.I. Fernandez-Dominguez, S.C. Heck, S.A. Maier, Chem. Rev. 111 (2011) 3888–3921.
[26] I. Cohanoshi, S. Yao, K.D. Belfield, F.E. Hernandez, J. Appl. Phys. 101 (2007) 086112.
[27] Y. Tsuboi, R. Shimizu, T. Shoji, N. Kitamura, J. Am. Chem. Soc. 131 (2009) 12623–12627.
[28] K. Ueno, S. Juodkazis, T. Shibuya, Y. Yokota, V. Mizekis, K. Sasaki, H. Misawa, J. Am. Chem. Soc. 130 (2008) 6928–6929.
[29] K. Ueno, S. Juodkazis, V. Mizekis, K. Sasaki, H. Misawa, Adv. Mater. 20 (2008) 26–30.
[30] K. Aslan, I. Gryczynski, J. Malicka, E. Matveeva, J.R. Lakowicz, C.D. Geddes, Curr. Opin. Biotech. 16 (2006) 55–62.
[31] J.R. Lakowicz, Plasmonics 1 (2006) 5–33.
[32] Y. Tian, T. Tatsuma, J. Am. Chem. Soc. 127 (2010) 2344–7637.
[33] E. Kowalska, B. Ohtani, Phys. Chem. Chem. Phys. 12 (2010) 4965–4971.
[34] J. Hohlfeld, S.-S. Wellershoff, J. Gudde, U. Conrad, V. Jahnke, E. Matthias, Chem. Phys. 251 (2000) 237–258.
[35] C. Bauer, J.-P. Abid, D. Fermin, H.H. Girault, J. Chem. Phys. 120 (2004) 9302–9315.
[36] A.L. Tchebotareva, P.V. Ruijgrok, P. Zijlstra, M. Orrit, Laser Photonics Rev. 4 (2010) 581–597.
[37] G.V. Hartland, Annu. Rev. Phys. Chem. 57 (2006) 403–430.
[38] S. Link, M.B. Burda, B. Mohamed, B. Nikoobakht, M.A. El-Sayed, J. Phys. Chem. A 103 (1999) 1165–1170.
[39] S. Link, M.B. Burda, B. Nikoobakht, M.A. El-Sayed, J. Phys. Chem. B 104 (2000) 6152–6163.
[40] R.R. Letfullin, C. Joenathan, T.F. George, V.P. Zharov, Nanomedicine 1 (2006) 473–480.
[41] V.K. Pustovalov, A.S. Smetannikov, V.P. Zharov, Laser Phys. Lett. 5 (2008) 775–792.
[42] V. Kotaidis, A. Plech, Appl. Phys. Lett. 87 (2005) 213102.
[43] V. Kotaidis, C. Dahmen, G. von Plessen, F. Springer, A. Plech, J. Chem. Phys. 124 (2006) 184702.
[44] J. Neumann, R. Brinkmann, J. Biomed. Opt. 10 (2005) 024001.
[45] D. Lapotko, Opt. Express 17 (2009) 2538–2556.
[46] J.M. Sun, B.S. Gerstman, B. Li, J. Appl. Phys. 88 (2000) 2352–2362.
[47] X. Wang, X. Xu, J. Therm. Stresses 25 (2002) 457–473.
[48] X. Michalet, F.F. Pinaud, L.A. Bentolila, J.M. Tsay, S. Doose, J.J. Li, G. Sundaresan, A.M. Wu, S.S. Gambhir, S. Weiss, Science 307 (2005) 538–544.
[49] V. Biju, T. Itoh, M. Ishikawa, Chem. Soc. Rev. 39 (2010) 3031–3056.
[50] J.P. Wilcoxon, J.E. Martin, F. Parsapour, B. Wiedenman, D.F. Kelley, J. Chem. Phys. 108 (1998) 9137–9143.
[51] J. Yguerabide, E.E. Yguerabide, Anal. Biochem. 262 (1998) 137–156.
[52] S. Schultz, D.R. Smith, J.J. Mock, D.A. Schultz, Proc. Natl. Acad. Sci. 97 (2000) 996–1001.
[53] M. Rycenga, C.M. Cobley, J. Zeng, W. Li, C.H. Moran, Q. Zhang, D. Qin, Y. Xia, Chem. Rev. 111 (2011) 3669.
[54] M.-C. Daniel, D. Astruc, Chem. Rev. 104 (2004) 293–346.
[55] H. Nabika, M. Takase, F. Nagasawa, K. Murakoshi, J. Phys. Chem. Lett. 1 (2010) 2470–2487.
[56] P.B. Johnson, R.W. Christy, Phys. Rev. B 6 (1972) 4370–4379.
[57] G. Mie, Ann. Phys. 25 (1908) 377–445. German version: http://diogenes.iwt.uni-bremen.de/vt/laser/papers/Mie-Beitrag-zur-Optik-AnnalenPhysik1908.PDF (accessed January 1, 2012), English version: http://diogenes.iwt.uni-bremen.de/vt/laser/papers/SAND78-6018-Mie-1908-translation.pdf (accessed January 1, 2012).
[58] A computational program, MiePlot: http://www.philiplaven.com/mieplot.htm (accessed January 1, 2012) can be conveniently used for the calculation of Cext, Cabs, and Csca.
[59] C. Soennichsen, T. Franzl, T. Wilk, G. Von Pressen, J. Feldmann, New J. Phys. 4 (2002) 93.
[60] A. Arbouet, D. Christofilos, N. Del Fatti, F. Vallee, J.R. Huntzinger, L. Arnaaud, P. Billaud, M. Boyer, Phys. Rev. Lett. 93 (2004) 127401.
[61] K.S. Lee, M.A. El-Sayed, J. Phys. Chem. B 109 (2005) 20331–20338.
[62] P.K. Jain, K.S. Lee, I.H. El-Sayed, M.A. El-Sayed, J. Phys. Chem. B 110 (2006) 7238–7248.
[63] B.J. Wiley, S.H. Im, Z.-Y. Li, J. McLellan, A. Siekkinen, Y. Xia, J. Phys. Chem. B 110 (2006) 15666–15675.
[64] M. Otter, Z. Phys. 161 (1961) 539–549.
[65] S. Link, M.A. El-Sayed, J. Phys. Chem. B 103 (1999) 4212–4217.
[66] T.S. Ahmadi, S.L. Logunov, M.A. El-Sayed, J. Phys. Chem. 100 (1996) 8053–8056.
[67] S.L. Logunov, T.S. Ahmadi, M.A. El-Sayed, J.T. Khoury, R.L. Whetten, J. Phys. Chem. B 101 (1997) 3713–3719.
[68] S. Link, C. Burda, Z.L. Wang, M.A. El-Sayed, J. Chem. Phys. 111 (1999) 1255–1264.
[69] O. Ekici, R.K. Harrison, N.J. Durr, D.S. Eversole, M. Lee, A. Ben-Yakar, J. Phys. D. Appl. Phys. 41 (2008) 185501.
[70] D. Werner, A. Furube, T. Okamoto, S. Hashimoto, J. Phys. Chem. C 115 (2011) 8503–8512.
[71] L. Anisimov, B.L. Kapeliovich, T.L. Perel'sman, Soviet Phys. JETP 39 (1974) 375–377.
[72] C.K. Sun, F. Vallee, L.H. Acioli, E.P. Ippen, J.G. Fujimoto, Phys. Rev. B 50 (1994) 15337–15348.
[73] F. Caupin, E. Herbert, C. R. Phys. 7 (2006) 1000–1017.
[74] B.J. Messinger, K. Ulrich, R.K. Chang, P.W. Barber, Phys. Rev. B 24 (1981) 649–657.
[75] C.F. Bohren, Am. J. Phys. 51 (1983) 323–326.
[76] R.K. Harrison, A. Ben-Yaker, Opt. Express 18 (2010) 22556–22571.
[77] J. Boneberg, J. Koenig-Birk, H.-J. Munzer, P. Leiderer, K.L. Shuford, G.C. Schatz, Appl. Phys. A 89 (2007) 299–303.
[78] K.L. Kelly, E. Coronado, L.L. Zhao, G.C. Schatz, J. Phys. Chem. B 107 (2003) 668–677.

[79] P.R. Sajanlal, C. Subramaniam, P. Sasanpour, B. Rashidian, T. Pradeep, J. Mater. Chem. 20 (2010) 2108–2113.
[80] S-S. Chang, C-W. Shih, C-D. Chen, W-C. Lai, C.R. Chris Wang, Langmuir 15 (1999) 701–709.
[81] S. Link, M.A. El-Sayed, J. Chem. Phys. 114 (2001) 2362–2368.
[82] P. Zijlstra, J.W.M. Chon, M. Gu, Phys. Chem. Chem. Phys. 11 (2009) 5915–5921.
[83] Ph. Buffat, J-P. Borel, Phys. Rev. A 13 (1976) 2287–2298.
[84] K. Dick, T. Dhanasekaran, Z. Zhang, D. Meisel, J. Am. Chem. Soc. 124 (2002) 2312–2317.
[85] K.K. Nanda, Pramana J. Phys. 72 (2009) 617–628.
[86] S. Inasawa, M. Sugiyama, Y. Yamaguchi, J. Phys. Chem. B 109 (2005) 3104–3111.
[87] H. Petrova, J.P. Juste, I. Pastoriza-Santos, G.V. Hartland, L.M. Liz-Marzan, P. Mulvaney, Phys. Chem. Chem. Phys. 8 (2006) 814–821.
[88] A. Plech, R. Cerna, V. Kotaidis, F. Hudert, A. Bartels, T. Dekorsy, Nano Lett. 7 (2007) 1026–1031.
[89] A. Plech, V. Kotaidis, C.S. Gresillon, C. Dahmen, G. von Plessen, Phys. Rev. B 70 (2004) 195423.
[90] A. Takami, H. Kurita, S. Koda, J. Phys. Chem. B 103 (1999) 1226–1232.
[91] S. Inasawa, M. Sugiyama, Y. Yamaguchi, J. Phys. Chem. B 109 (2005) 9404–9410.
[92] A. Pyatenko, M. Yamaguchi, M. Suzuki, J. Phys. Chem. C 113 (2009) 9078–9085.
[93] D. Werner, S. Hashimoto, T. Uwada, Langmuir 26 (2010) 9956–9963.
[94] P.V. Kamat, M. Fluminani, G.V. Hartland, J. Phys. Chem. B 102 (1998) 3123.
[95] K. Yamada, Y. Tokumoto, T. Nagata, F. Mafune, J. Phys. Chem. C 110 (2006) 11751–11756.
[96] K. Yamada, K. Miyajima, F. Mafune, J. Phys. Chem. C 111 (2007) 11246–11251.
[97] M. Shoji, K. Miyajima, F. Mafune, J. Phys. Chem. C 112 (2008) 1929–1932.
[98] H. Muto, K. Miyajima, F. Mafune, J. Phys. Chem. C 112 (2008) 5810–5815.
[99] F. Giammanco, E. Giorgetti, P. Marsili, A. Giusti, J. Phys. Chem. C 114 (2010) 3354–3363.
[100] D. Werner, S. Hashimoto, J. Phys. Chem. C 115 (2011) 5063–5072.
[101] G.W. Wang, Prog. Mater. Sci. 52 (2007) 648–698.
[102] S. Barcikowski, F. Devasa, K. Moldenhauer, J. Nanopart. Res. 11 (2009) 1883–1893.
[103] V. Amendola, M. Meneghetti, Phys. Chem. Chem. Phys. 11 (2009) 3805–3821.
[104] S. Sakamoto, M. Fujutsuka, T. Majima, J. Photochem. Photobiol. C Rev. 10 (2009) 33–56.
[105] N.G. Semaltianos, Crit. Rev. Solid State Mater. Sci. 35 (2010) 105–124.
[106] A. Plech, V. Kotaidis, M. Lorenc, J. Bonberg, Nat. Phys. 2 (2006) 44–47.
[107] J.H. Hodak, I. Martini, G.V. Hartland, J. Phys. Chem. B 102 (1998) 6958–6967.
[108] J.H. Hodak, A. Henglein, G.V. Hartland, J. Chem. Phys. 111 (1999) 8613–8621.
[109] P.B. Corkum, F. Brunel, N.K. Sherman, Phys. Rev. Lett. 61 (1988) 2886–2889.
[110] B.N. Chichkov, C. Momma, S. Nolte, F. Von Alvensleben, A.A. Tuennermann, Appl. Phys. A Mater. Sci. Process. 63 (1996) 109–115.
[111] W.A. Saunders, Phys. Rev. A 46 (1992) 7028–7041.
[112] U. Naeher, S. Bjornholm, S. Frauendorf, F. Garcias, C. Guet, Phys. Rep. 285 (1997) 245–320.
[113] Z. Lin, L.V. Zhigilei, Phys. Rev. B 77 (2008) 075133.
[114] L. Rayleigh, Philos. Mag. 5 (1882) 184–187.
[115] C. Novo, P. Mulvaney, Nano. Lett. 7 (2007) 520–524.
[116] S. Hashimoto, T. Uwada, M. Hagiri, R. Shiraishi, J. Phys. Chem. C 115 (2011) 4986–4993.
[117] O. Warshavski, L. Minai, G. Bisker, D. Yelin, J. Phys. Chem. C 115 (2011) 3910–3917.
[118] S. Ito, H. Yoshikawa, H. Masuhara, Appl. Phys. Lett. 80 (2002) 482–484.
[119] S. Ito, T. Mizuno, H. Yoshikawa, H. Masuhara, Jpn. J. Appl. Phys. 46 (2007) L241–L243.
[120] A. Ashkin, Phys. Rev. Lett. 24 (1970) 156–159.
[121] K. Svoboda, S.M. Block, Opt. Lett. 19 (1994) 930–932.
[122] Y. Tsuboi, T. Shoji, N. Kitamura, M. Takase, K. Murakoshi, Y. Mizumoto, H. Ishihara, J. Phys. Chem. Lett. 1 (2010) 2327–2333.
[123] M. Hu, G.V. Hartland, J. Phys. Chem. B 106 (2002) 7029–7033.
[124] S. Merabia, S. Shenogin, L. Joly, P. Keblinski, J-L. Barrat, Proc. Natl. Acad. Sci. 106 (2009) 15113–15118.
[125] V. Juve, M. Scardamaglia, P. Malioli, A. Crut, S. Marabia, L. Joly, N. Del Fatti, Phys. Rev. B 80 (2009) 195406.
[126] A. Plech, V. Kotaidis, M. Lorenc, M. Wulff, Chem. Phys. Lett. 401 (2005) 565–569.
[127] A. Siems, S.S.L. Weber, J. Boneberg, A. Plech, New J. Phys. 13 (2011) 043018.
[128] E.Y. Lukianova-Hleb, D.O. Lapotko, Nano Lett. 9 (2009) 2160–2166.
[129] E. Lukianova-Hleb, Y. Hu, L. Latterini, L. Tarpani, S. Lee, R.A. Drezek, J.H. Hafner, D.O. Lapotko, ACS Nano 4 (2010) 2109–2123.
[130] E.Y. Lukianova-Hleb, L.J.E. Anderson, S. Lee, J.H. Hafner, D.O. Lapotko, Phys. Chem. Chem. Phys. 12 (2010) 12237–12244.
[131] J. Neumann, R. Brinkmann, J. Appl. Phys. 101 (2007) 114701.
[132] J. Neunmann, R. Brinkmann, Appl. Phys. Lett. 93 (2008) 033901.
[133] H. Fujiwara, S. Yanagida, P.V. Kamat, J. Phys. Chem. B 103 (1999) 2589–2591.
[134] C.S. Ah, H.S. Han, K. Kim, D-J. Jang, Pure Appl. Chem. 72 (2000) 91–99.
[135] Z. Peng, T. Walther, K. Kleinermanns, Langmuir 21 (2005) 4249–4253.
[136] Y. Niidome, A. Hori, T. Sata, S. Yamada, Chem. Lett. 29 (2000) 310–311.
[137] H. Takahashi, Y. Niidome, T. Sato, S. Yamada, Colloid Surf. A 247 (2004) 105–113.
[138] T. Kawasawa, H. Takahashi, H. Kawasaki, Y. Niidome, S. Yamada, Trans. Mater. Res. Soc. Jpn. 30 (2005) 571–574.
[139] D. Werner, S. Hashimoto, T. Tomita, S. Matsuo, Y. Makita, J. Phys. Chem. C 112 (2008) 16801–16808.
[140] H. Wang, A. Piatenko, K. Kawaguchi, X. Li, Z. Swiatkowska-Warkocka, N. Koshizaki, Angew. Chem. Int. Ed. 49 (2010) 6361–6364.
[141] X. Li, A. Piatenko, Y. Shimizu, H. Wang, K. Koga, N. Koshizaki, Langmuir 27 (2011) 5076–5080.
[142] H. Wang, N. Koshizaki, L. Li, L. Jia, K. Kawaguchi, X. Li, A. Piatenko, Z. Swiatkowska-Warkocka, Y. Bando, D. Golberg, Adv. Mater. 23 (2011) 1865–1870.
[143] X. Li, N. Koshizaki, A. Piatenko, Y. Shimizu, H. Wang, J. Liu, X. Wang, M. Gao, Z. Wang, X. Zeng, Opt. Express 19 (2011) 12855.
[144] S. Pocovi-Martinez, M. Parreno-Romero, S. Agouram, J. Perez-Prieto, Langmuir 27 (2011) 5234–5241.
[145] J-P. Sylvestre, S. Poulin, A.V. Kabashin, E. Sacher, M. Meunier, J.H.T. Loung, J. Phys. Chem. B 108 (2004) 16864–16869.
[146] H. Hasegawa, N. Saitoh, K. Tsuji, K. Kimura, Z. Phys. D. 20 (1991) 325–327.
[147] N. Saitoh, H. Hasegawa, K. Tsujii, K. Kimura, J. Phys. Chem. 98 (1994) 2143–2147.
[148] K. Kimura, J. Phys. Chem. 98 (1994) 11997–12002.
[149] K. Kimura, Bull. Chem. Soc. Jpn. 69 (1996) 321–324.
[150] Y. Takeuchi, T. Ida, K. Kimura, J. Phys. Chem. B 101 (1997) 1322–1327.
[151] H. Eckstein, U. Kreibig, Z. Phys. D. 26 (1993) 239–241.
[152] S.V. Karpov, V.V. Slabko, G.A. Chiganova, Colloid J. 64 (2002) 425–441.
[153] H. Yoshikawa, T. Matsui, H. Masuhara, Phys. Rev. E 70 (2004) 061406.
[154] Y. Tanaka, H. Yoshikawa, T. Itoh, M. Ishikawa, Opt. Express 17 (2009) 18760–18767.
[155] Y. Zhang, C. Gu, A.M. Schwartzberg, S. Chen, J.Z. Zhang, Phys. Rev. B 73 (2006) 165405.
[156] S.H. Ko, Y. Choi, D.J. Hwang, C.P. Grigoropoulos, Appl. Phys. Lett. 89 (2006) 141126.
[157] K. Yamada, T. Itoh, Y. Tsuboi, Appl. Phys. Express 1 (2008) 087001.
[158] S. Hashimoto, T. Uwada, M. Hagiri, H. Takai, T. Ueki, J. Phys. Chem. C 113 (2009) 20640–20647.
[159] K. Furukawa, T. Kameyama, K. Okazaki, T. Yako, M. Otsuki, Y. Tsuboi, T. Torimoto, Chem. Lett. 40 (2011) 1411–1413.
[160] N.N. Nedyalkov, H. Takada, M. Obara, Appl. Phys. A 85 (2006) 163–168.
[161] N.N. Nedyalkov, T. Sakai, T. Mianishi, M. Obara, J. Phys. D. Appl. Phys. 39 (2006) 5037–5042.
[162] N.N. Nedyalkov, P.A. Atanasov, M. Obara, Nanotechnology 18 (2007) 305703.
[163] P. Leiderer, C. Bartels, J. Konig-Birk, M. Mosbacher, J. Boneberg, Appl. Phys. Lett. 85 (2004) 5370–5372.
[164] A. Kolloch, T. Geldhauser, K. Ueno, H. Misawa, J. Boneberg, A. Plech, P. Leider, Appl. Phys. A. 104 (2011) 793–799.
[165] A. Heltzel, S. Theppakuttai, S.C. Chen, J.R. Howell, Nanotechnology 19 (2008) 025305.
[166] D. Eversole, B. Luk'yanchuk, A. Ben-Yaker, Appl. Phys. A 89 (2007) 283–291.
[167] A. Plech, P. Leiderer, J. Boneberg, Laser Photon Rev. 3 (2009) 435–451.
[168] E. Boulais, A. Robitalle, P. Desjeans-Gauthier, M. Meunier, Opt. Express 19 (2011) 6177–6178.
[169] K. Ueno, S. Juodkazis, T. Shibuya, V. Mizeikis, Y. Yokota, H. Misawa, J. Phys. Chem. C 113 (2009) 11720–117249.
[170] K. Ueno, S. Takabatake, Y. Nishijima, V. Mizeikis, Y. Yokota, H. Misawa, J. Phys. Chem. Lett. 1 (2010) 657–662.
[171] K. Ueno, S. Takabatake, Y. Nishijima, V. Mizeikis, Y. Yokota, H. Misawa, Appl. Phys. Lett. 99 (2011) 011107.
[172] Y. Niidome, A. Hori, H. Yakahashi, Y. Goto, S. Yamada, Nano Lett. 1 (2001) 365–369.
[173] M. Kawasaki, M. Hori, J. Phys. Chem. B 107 (2003) 6760–6765.
[174] C-Y. Chen, J-Y. Fu-Ji Tsai, Y-C. Lu, Y-W. Kiang, C.C. Yang, Opt. Express 17 (2009) 14186–14198.
[175] C-H. Lin, L. Zhou, H. Xiao, S-J. Chen, H-L. Tsai, Opt. Lett. 35 (2010) 941–943.
[176] D.-Q. Yang, M. Meunier, E. Sacher, J. Appl. Phys. 95 (2004) 5023–5026.
[177] A. Keisow, S. Strojkark, K. Loeschner, A. Heilmann, A. Poldipensky, A. Abdolvand, G. Seifert, Appl. Phys. Lett. 86 (2005) 153111.
[178] J.E. Sipe, J.F. Young, J.S. Preston, H.M. van Driel, Phys. Rev. B 27 (1983) 1141–1154.
[179] Y. Shimotsuma, P.G. Kazansky, J. Qui, K. Hirao, Phys. Rev. Lett. 91 (2003) 247405.
[180] M. Hung, F. Zhao, Y. Cheng, N. Xu, Z. Xu, ACS Nano 3 (2009) 4062–4070.
[181] G. Obara, N. Maeda, T. Miyanishi, M. Terakawa, N.N. Nedyalkov, M. Obara, Opt. Express 19 (2011) 19093–19103.
[182] A. Habenicht, M. Olapinski, F. Burmeister, P. Leiderer, J. Boneberg, Science 309 (2005) 2043–2045.
[183] W. Huang, W. Qian, M.A. El-Sayed, J. Am. Chem. Soc. 128 (2006) 13330–13331.
[184] C. Tabor, W. Qian, M.A. El-Sayed, J. Phys. Chem. C 111 (2007) 8934–8941.
[185] R.G. Ispasoiu, L. Balough, O.P. Varnavski, D.A. Tomalia, T. Goodson III, J. Am. Chem. Soc. 122 (2000) 11005–11006.
[186] L. François, M. Mostafavi, J. Belloni, J-F. Delouis, J. Delaire, P. Feneyrou, J. Phys. Chem. B 104 (2000) 6133–6137.
[187] L. François, M. Mostafavi, J. Belloni, J.A. Delaire, Phys. Chem. Chem. Phys. 3 (2001) 4965–4971.
[188] L. Polavarapu, N. Venkatram, W. Ji, Q.-H. Xu, ACS Appl. Mater. Interface 1 (2009) 2298–2303.
[189] W. Sun, Q. Dai, J.G. Worden, Q. Huo, J. Phys. Chem. B 109 (2005) 20854–20857.
[190] G. Wang, W. Sun, J. Phys. Chem. B 110 (2006) 20901–20905.
[191] Y. Takeda, F. Mafune, T. Kondow, J. Phys. Chem. C 113 (2009) 5027–5030.

[192] Y. Takeda, T. Kondow, F. Mafune, Phys. Chem. Chem. Phys. 13 (2011) 586–592.
[193] G. Huttmann, B. Radt, J. Serbin, R. Birngruber, Proc. SPIE 5142 (2003) 88–95.
[194] E.Y. Lukianova-Helb, C. Santiago, D.S. Wagner, J.H. Hafner, D.O. Lapotko, Nanotechnology 21 (2010) 225102.
[195] E.Y. Lukianova-Helb, E.Y. Hanna, J.H. Hafner, D.O. Lapotko, Nanotechnology 21 (2010) 085102.
[196] S. Hashimoto, T. Uwada, H. Masuhara, T. Asahi, J. Phys. Chem. C 112 (2008) 15089–15093.
[197] S. Hashimoto, J. Phys. Chem. Lett. 2 (2011) 509–519.